University of California
Santa Barbara

Fabrication and Characterization of Gold Multi-Electrode Array Optimized for Spatially Resolved Electrochemical Aptamer-Based Sensing

A thesis submitted in partial satisfaction
of the requirements for the degree

Master of Science
in
Electrical and Computer Engineering

by

Oindrila Chatterjee

Committee in charge:

Professor Luke Theogarajan, Chair
Professor Kevin W. Plaxco
Professor Spencer L. Smith

March 2026

The Thesis of Oindrila Chatterjee is approved.

Professor Kevin W. Plaxco

Professor Spencer L. Smith

Professor Luke Theogarajan, Committee Chair

January 2026

Fabrication and Characterization of Gold Multi-Electrode Array Optimized for Spatially Resolved Electrochemical Aptamer-Based Sensing

by

Oindrila Chatterjee

Acknowledgements

I would like to express my heartfelt gratitude to my family and friends back in India for their constant encouragement and support throughout the course of this work. Their patience, understanding, and belief in me made this journey both possible and meaningful.

I am deeply grateful to my advisors, Prof. Luke Theogarajan, Prof. Kevin W. Plaxco, and Prof. Tod Kippin, for giving me the opportunity to work under their guidance. Their invaluable mentorship, guidance, and unwavering support helped me to learn and inspired me to broaden my horizons and deepen my thinking.

I would also like to thank Prof. Spencer L. Smith for serving on my thesis committee and for providing insightful feedback that strengthened this work.

Finally, I would like to thank those individuals without whom this project would not have been completed on time: Zachery Nelson, Shirshendu Chatterjee, Rose Mery Baktashin, Dallin Olster, and Kon Son. Their assistance, collaboration, and support during the critical phases of the project were invaluable, and their camaraderie made the research experience both productive and rewarding.

Abstract

Fabrication and Characterization of Gold Multi-Electrode Array Optimized for Spatially Resolved Electrochemical Aptamer-Based Sensing

by

Oindrila Chatterjee

This thesis focuses on the design, fabrication, and characterization of gold microelectrode array (MEA) devices for applications in electrochemical aptamer-based (EAB) sensing. EAB sensors leverage target-induced conformational changes in surface-bound aptamers to transduce molecular recognition phenomena into measurable electrochemical signals, enabling real-time, reversible, and reagentless detection of target molecules in complex biological environment. Such sensors are highly necessary for pharmacokinetic measurements, where continuous monitoring of target concentrations is required.

Motivated by the need to extend EAB sensing beyond single-point measurements toward spatially resolved target monitoring, this work develops planar, multi-site gold microelectrode arrays fabricated using standard microfabrication techniques. The MEAs were designed to support dense packing of sensing sites while maintaining well-defined electrode geometry and compatibility with aptamer functionalization. A custom PCB interface was developed to enable reliable electrical connections to external instrumentation.

Electrochemical characterization of the fabricated devices was performed using cyclic voltammetry and square-wave voltammetry to assess electrode quality, surface area, and stability before and after aptamer immobilization. Sensor performance was evaluated using kinetic differential measurements (KDM) to enhance signal robustness and suppress common-mode drift. The effects of electrode geometry, square wave frequency, and biological media on signal stability were analysed.

This thesis demonstrates that MEA based EAB sensors exhibit comparable electrochemical behavior and sensing performance to conventional gold wire electrode, while additionally enabling multi-site, spatially resolved measurements.

Importantly, this work also shows that planar gold microelectrode arrays can be functionalized with aptamers without electrochemical surface roughening while still achieving KDM responses comparable to electrochemically roughened gold wire control electrodes. This simplifies sensor fabrication while preserving robust EAB signaling, supporting the use of planar, microfabricated platforms for scalable EAB sensor implementations.Overall, this thesis lays the foundation for reproducible and scalable MEA-based platform for EAB sensing and for the future implementation of densely packed, minimally invasive sensor arrays capable of spatially resolved pharmacokinetic measurements real-time continuous in vivo monitoring.

Contents

Chapter 1

Introduction

1.1 Biosensors: Historical Perspective and Definition

Sensors have played an important role in improving the safety, efficiency, and quality of modern life, allowing the detection of physical and chemical changes such as pressure, motion, temperature, and electrical signals. Although often overlooked, sensors have continuously improved the efficacy and safety of everyday life [1].

The standard definition of 'biosensor' available from International Union of Pure and Applied Chemistry (IUPAC) is "A device that uses specific biochemical reactions mediated by isolated enzymes, immunosystems, tissues, organelles or whole cells to detect chemical compounds usually by electrical, thermal or optical signals" [2].

The conceptual foundations of electrochemical sensing date back to the early twentieth century. In 1906, M. Cremer demonstrated that the acidity of a solution could be measured via the electric potential across a glass membrane, establishing an early link between chemical activity and electrical signal transduction [3].

The field of biosensing emerged formally in 1956 when Leland C. Clark Jr. introduced the first enzyme-based electrode for oxygen detection, now widely referred to as the Clark

electrode [4]. This amperometric enzyme electrode laid the foundation for subsequent biosensors, including the development of the first glucose biosensor in 1962. These early innovations ultimately enabled the realization of medical biosensors such as real-time continuous glucose monitors, which have transformed diabetes management by allowing patients to independently monitor glucose levels and maintain euglycemic control [5].

Traditional analytical techniques for biomolecular identification and quantification include capillary electrophoresis [6], chromatographic methods such as liquid chromatography and gas chromatography coupled with mass spectrometry [7], and enzyme-linked immunosorbent assays (ELISA) [8]. While these methods are robust and highly sensitive, they typically require extensive sample preparation and are limited to discrete, end-point measurements. Moreover, they are generally unsuitable for continuous or in vivo monitoring [7].

Biosensors address these limitations by directly coupling a biological recognition element to a transducer, enabling rapid, selective, and potentially continuous measurements. Biosensors employ biological components such as enzymes, antibodies, aptamers, or nucleic acids to selectively recognize analytes and convert these recognition events into measurable signals[9]. As a result, biosensors have found broad application in biomedical diagnostics [10].

Figure 1.1 schematically illustrates the key parts of a typical biosensor: (a) bioreceptors that selectively bind to the target analyte; (b) an interface architecture where a specific biological recognition event occurs and generates a measurable signal; (c) a transducer element that converts this event into a physical signal, such as a change in electrical current at an electrode.

The transducer output is subsequently converted into an electronic signal, amplified by a detector circuit using an appropriate reference, and transmitted for processing by (d) computer software, where it is transformed into a meaningful parameter describing the

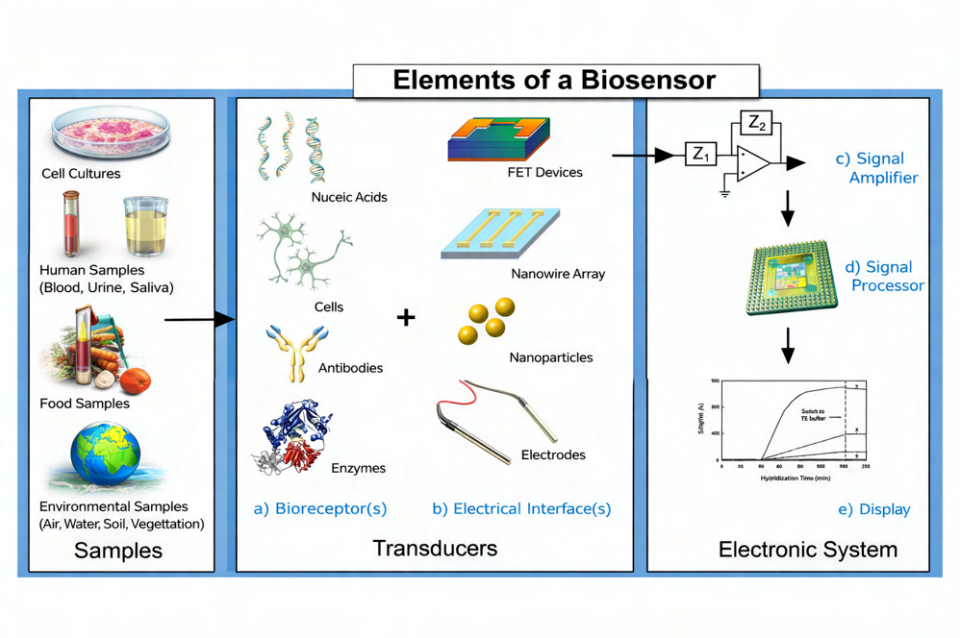

Figure 1.1: Schematic illustration of biosensor comprising three components: detector, transducer and output system.[6]

process under investigation. Finally, the processed information is presented to the user through (e) a human–machine interface. Biosensors can be applied to a wide range of samples, including body fluids, food samples, cell cultures, and environmental samples[6].

With healthcare shifting towards early diagnostics and personal health management, increasing attention has been focused on direct biomarker detections and their applications in diagnostics, especially in point-of-care devices [11, 12, 13]. The main goal in biomarker-based diagnostics is to quickly collect information from as many biomarkers as possible and to analyze them for a global overview of the patient's health condition. This task requires fast, miniaturizable and easy-to-use devices, preferable with the capability of multiplex detection [14, 15]. One important area of the research currently being carried out for this purpose is biosensors [6, 7, 8].

1.2 Emergence of Electrochemical Biosensors

Electrochemical biosensors emerged as a powerful analytical platform by coupling molecular recognition events to electrical signal transduction at an electrode–electrolyte interface. In a general biosensor architecture, a biorecognition element interacts selectively with a target analyte and undergoes physicochemical changes that are subsequently converted into a measurable signal by a transducer. When the transducer is electrochemical in nature, these changes are reflected as variations in electrical parameters such as current, potential, charge, or impedance, ideally in proportion to the analyte concentration [6, 15].

Over the past several decades, electrochemical biosensors have attracted significant research interest due to their high sensitivity, rapid response, label-free detection capability, and low instrumentation cost [6, 9]. Importantly, electrochemical transduction is inherently surface-sensitive and does not require optical access, making it compatible with opaque or complex biological media. The versatility of biosensors allows biorecognition elements to be integrated into different systems for both in vivo and in vitro sensing. These attributes, together with favorable scaling behavior upon electrode miniaturization, have made electrochemical biosensors ideal for portable, point-of-care, and implantable diagnostic technologies [6, 7, 8].

An electrochemical biosensor is a biosensor with an electrochemical transducer [6]. A wide range of electrochemical measurement techniques, including voltammetric, impedimetric, chronocoulometric, and potentiometric methods have been employed to translate molecular binding events into electrical signals, forming the theoretical foundation for modern electrochemical biosensing platforms [6, 15]. This versatility has enabled electrochemical biosensors to be adapted to diverse biological recognition elements and sensing environments, laying the groundwork for advanced affinity-based and real-time biosensing technologies discussed in subsequent sections.

1.3 Electrochemical Aptamer-Based (EAB) Biosensors

Electrochemical aptamer-based (EAB) biosensors are a class of biosensors that combine the molecular recognition capability of aptamers with electrochemical signal transduction at an electrode–electrolyte interface. In these systems, target binding events are converted directly into measurable electrical signals. Unlike traditional biosensors that rely on irreversible binding or multi-step labeling procedures, EAB sensors are designed to operate through reversible, binding-induced modulation of electron transfer, enabling continuous and real-time sensing [10, 16, 17, 18].

EAB sensors have gained significant attention due to their high sensitivity, operational simplicity, and compatibility with miniaturized electrochemical platforms. Their reagentless operation and electrical readout make them particularly attractive for use in complex biological environments, where optical methods or sample-intensive analytical techniques are often impractical [11, 14]. Electrochemical, aptamer-based sensors are composed of a redox-reporter-modified, electrode-bound aptamer. The binding of the target molecule to this receptor induces a conformational change that, in turn, reduces the efficiency with which the redox reporter approaches the electrode to transfer electrons. The resulting change in electron transfer kinetics is easily measured using various electrochemical methods.

1.3.1 Aptamers as Biorecognition Elements

Aptamers are short, single-stranded DNA or RNA oligonucleotides selected in vitro for their ability to bind specific molecular targets with high affinity and selectivity using the systematic evolution of ligands by exponential enrichment (SELEX) process. Aptamers

can be engineered to recognize a wide range of targets, including small molecules, proteins, and ions, and offer several advantages over antibodies, such as chemical stability, low immunogenicity, ease of synthesis, and reproducible batch-to-batch fabrication [16, 17].

A key feature that makes aptamers particularly suitable for electrochemical sensing is their ability to undergo predictable conformational or dynamic changes upon target binding. These binding-induced structural rearrangements can be transduced into electrical signals when the aptamer is tethered to an electrode surface, forming the basis of EAB sensor operation [10].

1.3.2 Surface Functionalization

In a canonical EAB sensor configuration, aptamers are immobilized onto a gold working electrode via thiol–gold chemistry. Thiol-modified aptamers spontaneously form strong covalent-like bonds with gold surfaces, resulting in a stable and well-defined probe layer. To optimize sensor performance, the electrode surface is typically passivated using a mixed self-assembled monolayer (SAM) composed of the aptamer and short chain alkanethiols, such as mercaptohexanol (MCH) [10, 15].

This mixed SAM architecture serves several critical functions: it reduces nonspecific adsorption of biomolecules, controls aptamer packing density, improves probe orientation, and stabilizes the electrode–electrolyte interface. Proper passivation is essential for achieving reproducible electron-transfer kinetics and minimizing signal drift, particularly during prolonged measurements in biological fluids [10, 15]. Gold remains the preferred electrode material for EAB sensors due to its chemical inertness and the extensive understanding of thiol-based surface chemistry.

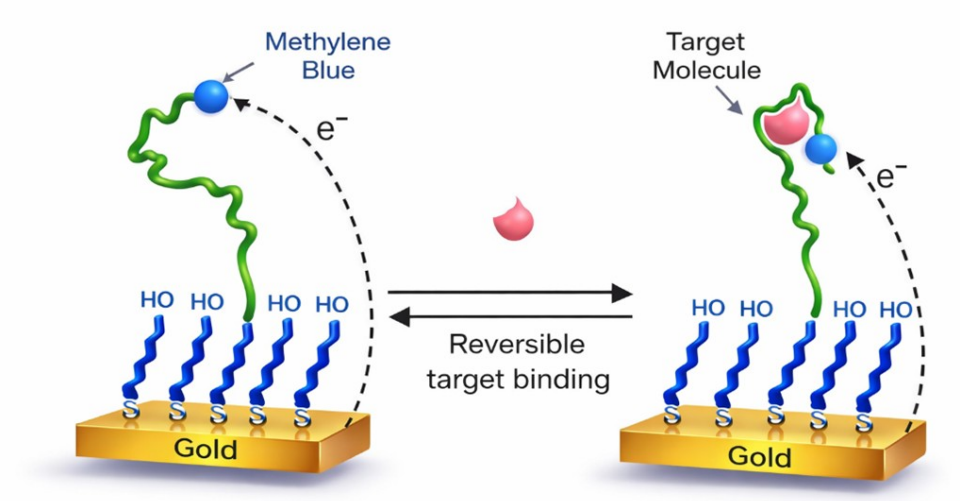

Figure 1.2: Schematic illustration of Electrochemical aptamer-based sensors. They are composed of a redox-reporter-modified, electrode-bound aptamer. The binding of the target molecule to this receptor induces a conformational change that, in turn, reduces the efficiency with which the redox reporter approaches the electrode to transfer electrons. The resulting change in electron transfer kinetics is easily measured using a variety of electrochemical methods.[18]

1.3.3 Signal Generation Mechanism in EAB Sensors

To generate an electrochemical signal, EAB sensors employ a redox reporter like methylene blue or ferrocene, covalently attached to the aptamer. The electrochemical response arises from electron transfer between this redox reporter and the electrode surface as shown in Fig. 1.2. In the absence of a target, the aptamer occupies a dynamic ensemble of conformations that defines a baseline electron-transfer rate. Upon target binding, changes in aptamer conformation or dynamics alter the effective distance or collision frequency of the redox reporter relative to the electrode, leading to a measurable change in electrochemical signal [10, 17].

Because this signaling mechanism is reversible and does not require external reagents, EAB sensors are well suited for repeated and continuous measurements, distinguishing them from many traditional affinity-based biosensing approaches [11].

1.3.4 Electrochemical Measurement Methods

Electrochemical aptamer-based biosensors are commonly use voltammetric and impedimetric techniques, which provide sensitive and quantitative readouts of binding-induced changes at the electrode–electrolyte interface. Voltammetric methods, such as cyclic voltammetry and square-wave voltammetry, are frequently used to monitor the redox response of reporter molecules tethered to the aptamer. In these approaches, target binding alters the efficiency of electron transfer between the redox reporter and the electrode, resulting in measurable changes in current that reflect the aptamer–target interaction [10, 17].

Electrochemical impedance spectroscopy provides a complementary interrogation strategy by probing changes in interfacial impedance associated with aptamer binding and surface modification. Binding events can modulate charge-transfer resistance or interfacial capacitance, enabling label-free detection and surface characterization [6, 15].

After data acquisition, concentration-dependent responses obtained from electrochemical measurements are analyzed using the Langmuir-Hill binding isotherm model, to extract quantitative affinity parameters including the dissociation constant [10, 13, 14, 19].

In addition to equilibrium analysis, signal processing plays an important role in ensuring reliable sensor performance, particularly during long-term measurements. Advanced signal-processing strategies have been developed to improve measurement stability and suppress signal drift in electrochemical aptamer-based sensors, especially when operating in complex biological environments. Such approaches enhance robustness without altering the underlying sensing chemistry and are essential for translating EAB sensors toward continuous and in vivo applications [11, 17].

1.4 Microelectrode Arrays

1.4.1 Introduction

Microelectrode arrays (MEAs) are devices that integrate multiple individually microelectrodes on a single substrate, allowing parallel electrochemical measurements from spatially distributed sites [6, 7, 8]. Unlike single macroelectrodes, MEAs support miniaturization to achieve compact and scalable architectures in which electrode geometry, such as size, shape, and spacing, is precisely defined through fabrication. This precise geometric control enables reproducible electrochemical behavior across electrodes and devices, which is critical for biosensing applications that require consistent performance across multiple sensing sites[7].

MEAs have been widely adopted in neural recording and stimulation, analytical electrochemistry, and biosensing due to their ability to combine high spatial resolution with rapid temporal response [8, 14]. In electrochemical biosensing, MEAs represent an evolution from single-electrode platforms toward systems capable of multiplexed and spatially resolved measurements while maintaining compatibility with established surface chemistries and interrogation methods [4, 7, 15].

A wide variety of MEA architectures have been reported, reflecting differences in target application, implantation strategy, and required spatial resolution. Fig. 1.3 shows different architectures of microelectrodes used for neural and biosensing [20]. Planar MEAs, fabricated on glass or silicon substrates, consist of laterally distributed microelectrodes and are widely used for in vitro sensing and surface-based electrochemical measurements due to their ease of fabrication and integration with microfluidic systems [8, 9]. Penetrating MEAs, such as Utah-style arrays and Michigan-style probes, extend microelectrodes vertically into tissue, enabling depth-resolved measurements and localized interrogation of chemical gradients in biological environments [21, 22, 23]. Other configurations,

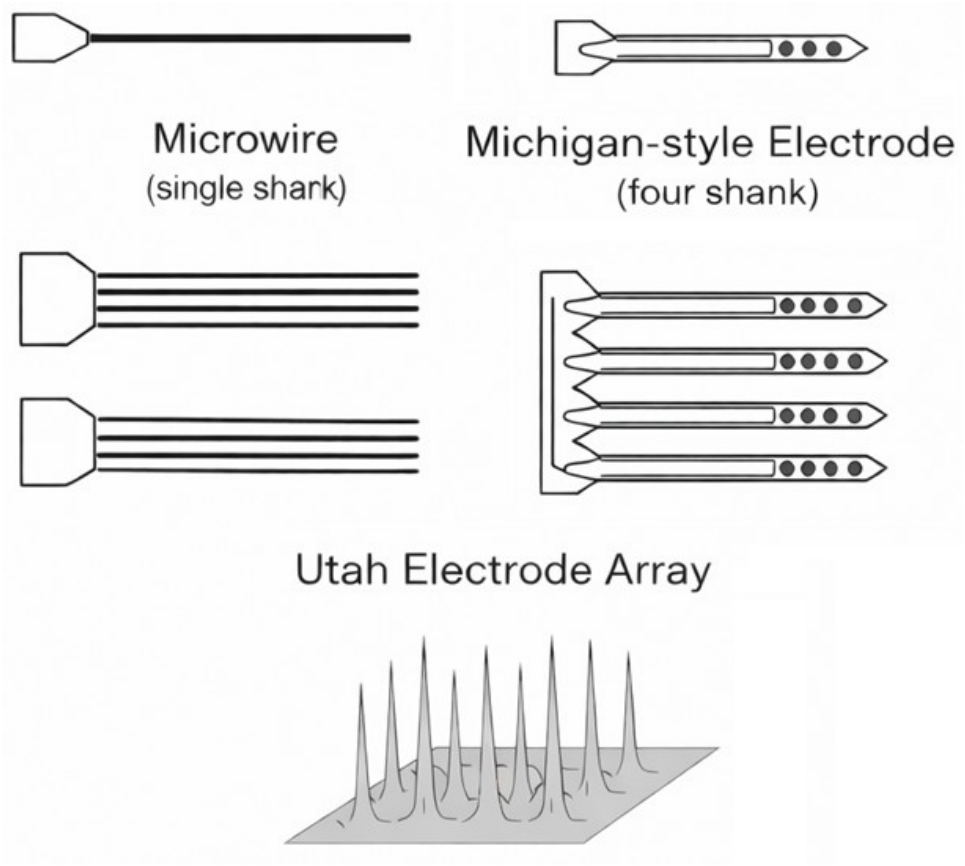

Figure 1.3: . Schematic illustration of different architectures of neural and biosensing microelectrode arrays.[20]

including microwire bundles and conical microelectrodes, offer alternative trade-offs between mechanical compliance, spatial density, and fabrication complexity [22, 24].

Beyond scalability, the electrochemical behavior of microelectrodes differs fundamentally from that of macroelectrodes. When electrode dimensions are reduced to the micrometer scale, mass transport transitions toward radial diffusion, resulting in faster establishment of steady-state currents and reduced capacitive charging effects. These properties enable improved temporal resolution, enhanced signal stability, and reduced sensitivity to convective disturbances, which are particularly advantageous for measurements in complex biological environments [6, 7, 8].

Importantly, MEAs also enable architectural integration that is difficult to achieve

with discrete electrodes. Lithographic fabrication allows precise placement of working, reference, and counter electrodes on the same substrate, along with defined passivation and routing layers [8, 15]. This integration facilitates compact device footprints, reduces wiring complexity, and supports multiplexed measurements without increasing invasiveness. Such attributes have positioned MEAs as key enabling platforms for advanced biosensing strategies, including multi-analyte detection and spatially resolved molecular monitoring [7, 14].

1.4.2 Role of Microelectrode Array in Biosensing

Microfabricated electrodes play a foundational role in modern biosensing by providing control over electrode geometry, surface properties, and spatial organization, parameters that directly influence sensor sensitivity, stability, and temporal performance. Microfabrication enables deterministic definition of electrode size, shape, and spacing, allowing biosensor behavior to be engineered with high reproducibility. This is important for biosensing platforms operating in complex biological environments, where signal fidelity and consistency across sensing sites are important [1, 6, 25].

Polymer dielectrics and passivation layers play a critical role in implantable and bio-interfaced electronic systems by electrically isolating interconnects while maintaining mechanical compliance and long-term stability in physiological environments. Recent reviews of flexible and wireless neural electronics highlight materials such as benzocyclobutene (BCB), polyimide, and parylene as enabling technologies for chronic bioelectronic interfaces due to their favorable dielectric and packaging properties[26, 27, 28].

At the microscale, electrode geometry strongly affects mass transport and interfacial processes that govern signal generation in biosensors. Reduced electrode dimensions enhance radial diffusion and shorten characteristic diffusion lengths, enabling faster

response times and improved temporal resolution compared to macroelectrodes [6, 15]. In addition, smaller electrode active areas reduce background capacitive currents, improving signal-to-noise ratios and enabling more reliable detection of surface-confined biochemical interactions. These characteristics are advantageous across a wide range of biosensing modalities, including enzymatic, affinity-based, and nucleic-acid-based sensors [3, 7].

Microfabrication further enables the integration of biosensing electrodes with insulating passivation layers and on-chip routing, isolating only the active sensing areas while minimizing parasitic electrochemical contributions from interconnects. This architectural control is essential for reliable surface functionalization with self-assembled monolayers, aptamers, or other biorecognition elements, ensuring that sensing occurs exclusively at well-defined interfaces [10, 15]. As a result, microfabricated electrodes provide a robust and scalable platform for translating molecular recognition into stable, quantitative electrochemical signals.

Conventional gold wire electrodes have been widely used in electrochemical biosensing, including EAB sensors, due to their chemical inertness, ease of functionalization via thiol–gold chemistry, and compatibility with established electrochemical interrogation methods [6, 10]. Despite these advantages, gold wire electrodes intrinsically support only single-point electrochemical measurements, limiting their ability to capture spatial variations in analyte concentration. A representative gold wire–based three-electrode configuration is shown in Fig. 1.4.

Many biologically relevant molecules, including therapeutic drugs and metabolites, exhibit spatially heterogeneous concentration profiles in tissue due to nonuniform diffusion, localized binding, vascular transport, and clearance mechanisms. Spatial pharmacokinetic measurements require the ability to monitor analyte concentrations simultaneously at multiple, well-defined locations within a biological environment. Conventional pharmacokinetic measurements, which rely on bulk sampling or single-point sensing, average

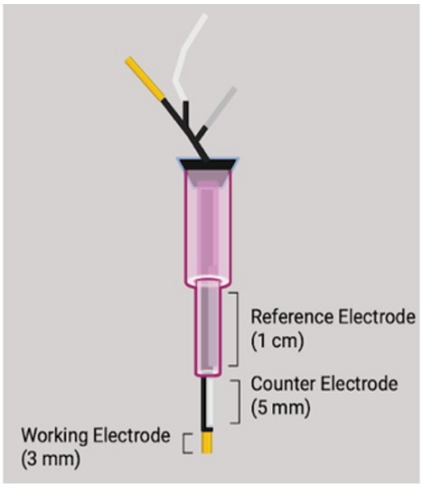

Figure 1.4: Schematic of a conventional three-electrode configuration EAB sensor.

these gradients and obscure localized concentration dynamics that can be critical for efficacy and toxicity assessment.

Microelectrode arrays (MEAs) directly enable this capability by integrating multiple independently addressable sensing sites with precisely controlled spatial separation on a single platform. This capability is particularly important for understanding drug transport in vivo, where concentration profiles can vary significantly over millimeter and submillimeter length scales.

By maintaining identical electrode geometries and surface chemistries across the array, MEAs ensure that observed signal differences arise from true spatial variations in analyte concentration rather than electrode-to-electrode variability. In addition, the microscale dimensions of MEA electrodes support rapid temporal response, allowing spatial pharmacokinetic measurements to be resolved in real time as concentration fronts evolve. Together, these attributes position MEA-based biosensing platforms as powerful tools for transforming traditional bulk pharmacokinetic measurements into spatially resolved, site-specific analyses that more accurately reflect molecular transport and distribution in complex biological systems.

1.5 Goal and Outline of the Thesis

This thesis focuses on improving electrochemical biosensing technologies for real-time, spatially resolved molecular monitoring in complex biological environments. In particular, the work aims to advance EAB sensing platforms by transitioning from conventional single-electrode configurations to microfabricate MEA architectures.

The primary goal of this thesis is to design, fabricate, and characterize gold microelectrode arrays optimized for spatially resolved EAB sensing, enabling simultaneous multi-site measurements and improved experimental control. This thesis will discuss the improvements that have been made in each of those areas and the challenges faced during this work.

In Chapter 2, the design constraints and microfabrication workflow of gold microelectrode arrays are discussed.

In Chapter 3, the electrochemical functionalization, sensing performance, and data analysis of the fabricated microelectrode arrays are described. The performance of MEA-based sensors is evaluated in comparison to conventional gold wire electrodes, with emphasis on signal stability, reproducibility, and spatially resolved molecular measurements.

In Chapter 4, the contents of this thesis are summarized and future work is proposed for this project.

Chapter 2

Design and Microfabrication of Gold Microelectrode Arrays for EAB Sensing

2.1 Microelectrode Arrays for Bioelectronic and Electrochemical Sensing

Microelectrode array (MEA) has played an important role in the development of implantable bioelectronic interfaces, particularly for neural recording and stimulation. Early silicon-based neural probes demonstrated that microfabrication techniques could be used to integrate multiple microscale electrodes on rigid substrates with high spatial precision, enabling simultaneous electrical measurements across distributed regions of neural tissue [21, 24]. These foundational studies established the feasibility of batch-fabricated, multi-site electrode systems and laid the groundwork for modern MEA technologies.

Subsequent advances in thin-film processing, photolithography, and dielectric passiva-

tion enabled increasingly dense electrode layouts, improved routing of metal interconnects, and mechanically robust substrates suitable for chronic implantation [22, 23]. More recent work has explored ultrathin silicon probes and polymer-passivated architectures to reduce device footprint and improve mechanical compliance while maintaining precise control over electrode geometry and placement [23, 25, 29].

Despite these advances, most conventional MEAs have been primarily optimized for electrophysiological measurements, where design considerations are dominated by electrode impedance, thermal noise, and charge transport capacity. As a result, such devices generally use small electrode areas and geometries that are not ideal for electrochemical sensing. Limited geometric surface area and high interfacial impedance can significantly constrain faradaic current levels, reducing signal-to-noise ratios during voltammetric interrogation and limiting sensitivity for molecular detection.

In parallel, increasing attention has been directed toward adapting microfabricated electrode platforms for chemical and molecular sensing. Noble metal electrodes, particularly gold, offer favourable electrochemical stability and surface chemistry compatibility for biosensing applications, including thiol-based self-assembled monolayers (SAMs) used to immobilize molecular recognition elements [8, 16]. Benzocyclobutene (BCB) was used as polymer passivation layer in this thesis. BCB was selected as the passivation dielectric due to its low dielectric constant, excellent planarization characteristics, chemical stability, and established use in implantable and biomedical microsystems [27, 28]. BCB has been widely employed in neural and retinal prosthesis platforms, where it serves as a robust polymer dielectric and encapsulation layer compatible with microelectrode array fabrication and long-term biological operation.[22, 27, 28]

Recent in vivo studies have further highlighted the importance of spatially resolved molecular sensing within complex biological environments. Measurements of therapeutic drug concentrations within the brain have revealed pronounced spatial heterogeneity

that cannot be captured by bulk sampling techniques such as plasma measurements or microdialysis [11, 17]. These findings underscore the need for implantable sensing platforms capable of resolving molecular concentration dynamics across multiple spatial locations simultaneously.

Electrochemical aptamer-based (EAB) sensors offer a promising route toward such measurements by enabling real-time, reversible detection of target molecules directly within biological tissues. However, EAB sensor performance is strongly dependent on electrode material selection, exposed surface area, and passivation integrity, as signal transduction relies on thiol-on-gold monolayer formation and frequency-dependent electron-transfer kinetics [1, 10].

Together, these considerations motivate the development of a custom microfabricated gold MEA platform specifically optimized for spatially resolved EAB sensing, rather than direct reuse of electrophysiology-focused MEA architectures.

Microfabrication processes enable the production of devices with feature sizes ranging from the micrometer to the millimeter scale. A key advantage of these processes is their ability to fabricate large numbers of electrodes in parallel, which not only reduces fabrication cost but also enables the production of electrode arrays with highly uniform and reproducible surface properties[21, 22]. Such batch fabrication is particularly important for electrochemical sensing applications, where variations in electrode surface chemistry can lead to device-to-device variability in performance [12]. In this thesis, gold electrodes were fabricated using standard microfabrication techniques to ensure reproducibility, scalability, and compatibility with electrochemical aptamer-based sensing.

2.2 Design and Fabrication of the Gold Microelectrode Array

This section describes the design and fabrication of the gold microelectrode arrays developed in this thesis. The devices incorporate planar gold working electrodes of two different diameters implemented on a single microfabricated platform to enable controlled comparison of electrode surface area effects in electrochemical aptamer-based sensing, while also testing the suitability of microfabricated electrodes for spatially resolved pharmacokinetic measurements[11, 17].

2.2.1 Working Electrode Geometry Design

A schematic top-view layout of the microelectrode array, illustrating the working electrodes, interconnect routing, contact pads, and shank geometry, is shown in Fig. 2.1. Two working electrode diameters were explored in this work: 1500 μm and 500 μm, corresponding to the CAD layouts shown in Fig. 2.2(a) and Fig. 2.2(b), respectively.

The 1500 μm diameter electrodes were designed to closely match the geometric surface area of the gold wire working electrodes used in prior electrochemical aptamer-based sensor studies [10, 11, 17]. The reference gold wire electrodes consist of approximately 3 mm of exposed length with a diameter of 200 μm, corresponding to an estimated geometric surface area of approximately 1.9 mm^2. The 1500 μm planar circular electrodes provide a comparable surface area, enabling direct comparison between microfabricated planar electrodes and conventional wire-based working electrodes while minimizing changes to aptamer packing density and electrochemical signal magnitude [10, 12, 13].

To investigate whether EAB sensors can still detect targets effectively when the electrode size is reduced, a second electrode geometry with a 500 μm diameter was

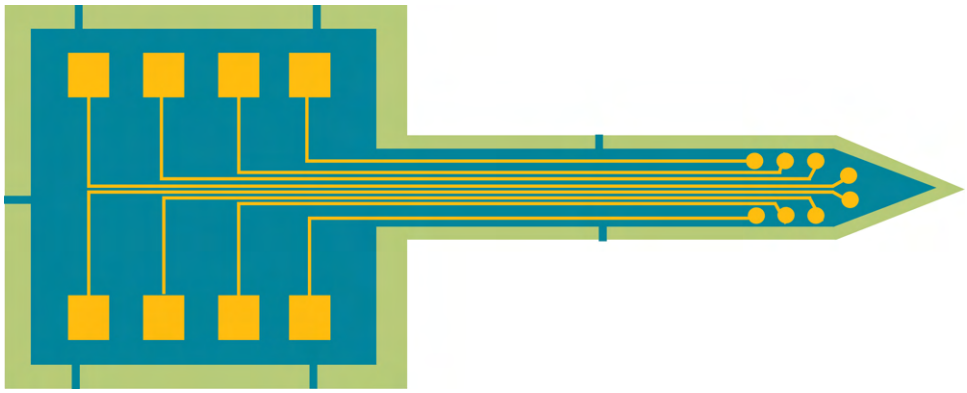

Figure 2.1: Schematic layout of the gold microelectrode array design.

implemented. This reduced-area design was intended to assess the feasibility of lowering electrode footprint while preserving measurable faradaic currents and stable sensor performance. Such a reduction in electrode size is particularly relevant for future applications requiring higher spatial resolution or denser electrode integration. Reducing electrode dimensions while maintaining sensing functionality is particularly relevant for future in vivo implementations, where spatial heterogeneity in drug distribution necessitates multiple closely spaced sensing sites to resolve local pharmacokinetic dynamics [11, 17].

In both designs, the working electrodes were connected to enlarged contact pads via thin-film gold interconnects, with only the active electrode regions exposed to the electrolyte through patterned passivation layers. For the 1500 μm diameter electrode, the contact pads were 3 mm × 3 mm, and the device incorporated a shank of $\sim$ 16.2 mm length and 5 mm width, resulting in an overall electrode footprint of $\sim$ 33.3 mm × 12.6 mm. For the 500 μm diameter electrode, the contact pads were reduced to approximately 2 mm × 2 mm, with a corresponding shank length and width of approximately 5.96 mm and 1.5 mm, yielding a total electrode footprint of approximately 18.7 mm × 7.3 mm.

Overall, this electrode geometry design enabled systematic evaluation of surface-area-dependent effects in electrochemical aptamer-based sensing while preserving a consistent device architecture and fabrication process. This approach also provides a scalable

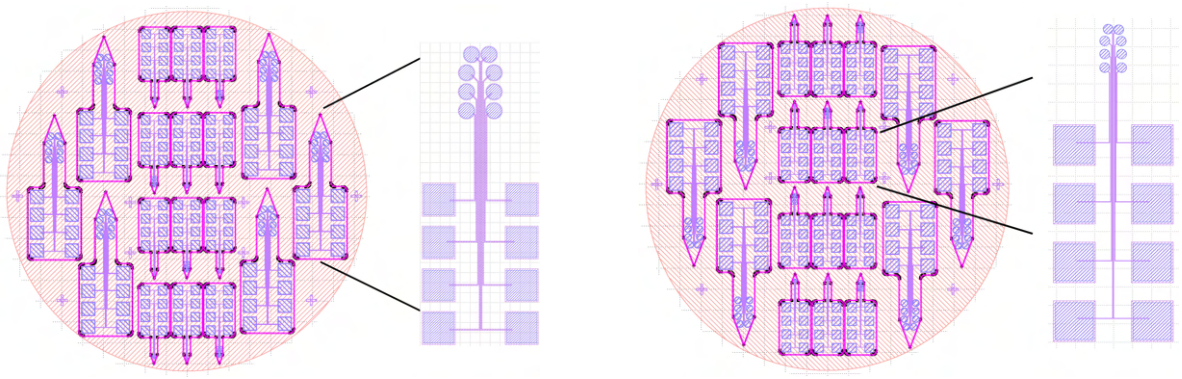

(a) (b)

Figure 2.2: Mask layout—CAD layout of two different electrode geometries of the MEA: (a) mask having electrodes of diameter 1500 μm and (b) mask having electrodes of diameter 500 μm.

foundation for future implementation of spatially resolved pharmacokinetic measurements using microfabricated electrode arrays[11, 12, 17, 30].

2.2.2 Fabrication Methodology

This section describes the microfabrication process used to realize the gold microelectrode arrays presented in this thesis. Standard cleanroom-compatible microfabrication techniques were employed to ensure reproducibility, dimensional control, and compatibility with electrochemical sensing in aqueous environment[31, 32]. The fabrication process includes wafer preparation, metal patterning for electrodes and interconnects, dielectric passivation, and definition of exposed electrode regions, resulting in fully functional microelectrode arrays suitable for electrochemical aptamer-based sensing.

2.2.2.1 Metallization and Patterning of Gold Electrodes

The fabrication process began with n-doped, single-side polished Si (100) wafers with a thickness of $\sim 340\ \mu m$. Schematic illustration of the process flow is shown in Fig. 2.3. To electrically isolate the metal electrodes from the silicon substrate, a 200 nm thin Low

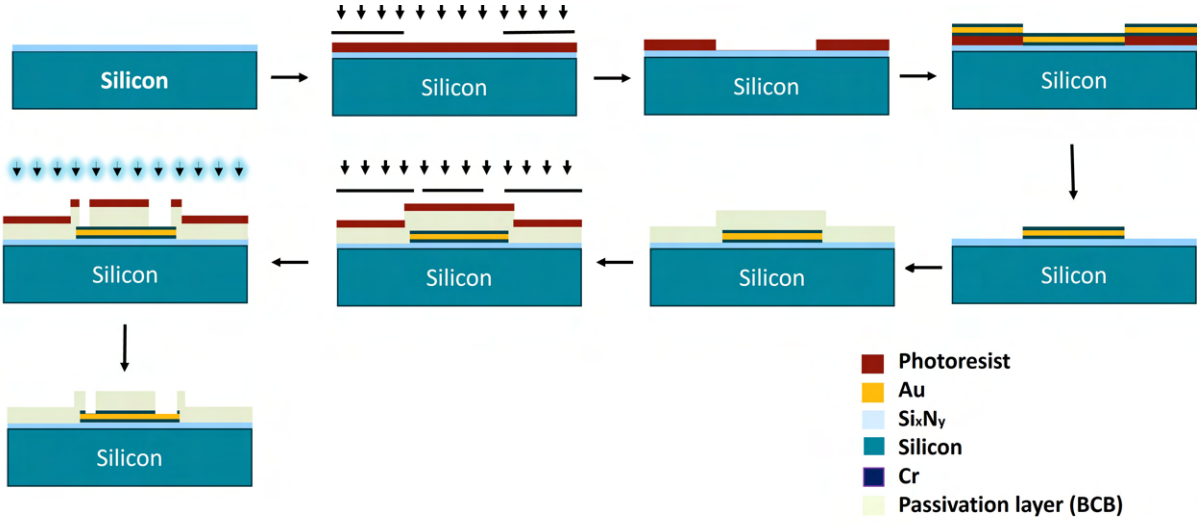

Figure 2.3: Schematic illustration of the microfabrication process flow for metallization and patterning of planar gold microelectrode arrays.

Stress (LS) Si_xN_y dielectric layer was deposited by plasma-enhanced chemical vapor deposition (PECVD) at a rate of 12.3 nm/min for 16 min 15 s. PECVD Si_xN_y is widely used in microelectrode fabrication due to its chemical robustness, low defect density, and compatibility with thin-film electrochemical devices [21, 23, 31].

The electrode sensing sites, contact pads, and interconnect traces were patterned using standard photolithography. An adhesion promoter (SurPass 4000) was puddled to enhance photoresist adhesion to the underlying Si_xN_y dielectric surface. Positive photoresist (SPR 220-3.0) was then spin-coated at 2.5 krpm for 30 s, resulting in a resist thickness of approximately 3 μm, followed by a soft-bake and backside cleaning. The electrode sensing sites, contact pads, and interconnect traces were patterned using a maskless laser aligner (MLA) at an exposure dose of 200 $\mu C/cm^2$, a parameter critical for pattern quality. Post-exposure bake was subsequently performed to stabilize the patterned resist. To improve the resist profile for metal lift-off, the exposed wafers were soaked in toluene prior to development, a technique known to induce surface hardening and promote the formation of a slight resist undercut favorable for lift-off processes[33]. The resist

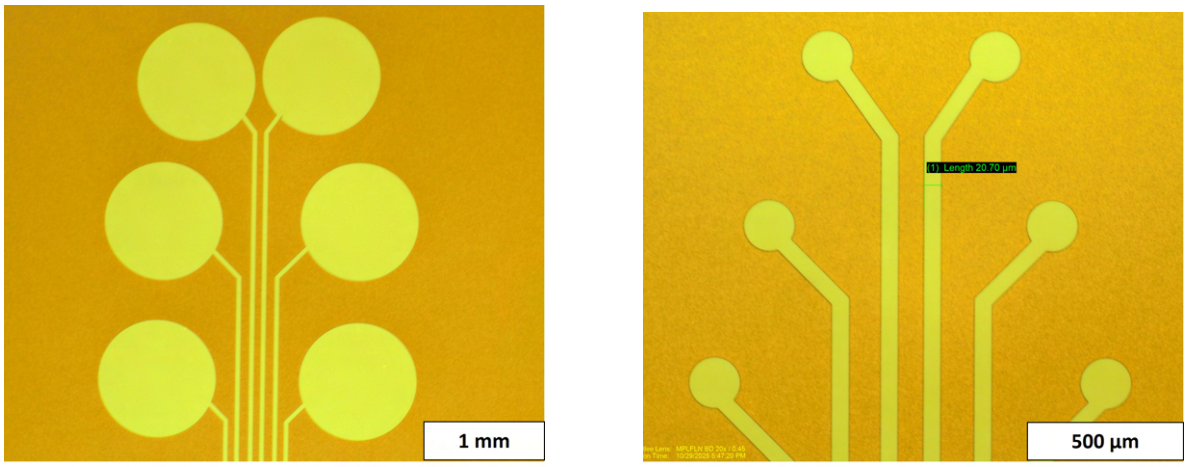

(a) (b)

Figure 2.4: Patterns of electrode sensing sites post photolithography for (a) 1500 μm electrode diameter and (b) 500 μm electrode diameter.

patterns were then developed using AZ300 MIF for 120 s. The wafers post-lithography are shown in Fig. 2.4.

After lithographic patterning, Cr/Au/Cr metal stack with thicknesses of 20 nm / 200 nm / 20 nm, respectively, was deposited using electron-beam evaporation. Chromium was used as the adhesion layer due to its strong adhesion to silicon nitride and its high resistance to electrochemical cleaning processes, as discussed in a later section. The top chromium layer promoted adhesion to subsequent polymer passivation layers. Lift-off was then performed to remove excess metal, leaving behind well-defined gold electrodes, interconnects, and contact pads as shown in Fig. 2.5.

Following metallization, benzocyclobutene (BCB, Cyclotene™ 3046) was used as a polymer passivation layer to electrically insulate the metal interconnects and contact regions while leaving the working electrode sites open. Prior to BCB deposition, adhesion promoter AP3000 was spin-coated and soft-baked to enhance adhesion to the underlying metal. The BCB layer was then spin-coated using a multi-step spin program (500 rpm spread, 5000 rpm coating, followed by low-speed leveling and drying steps). After which,

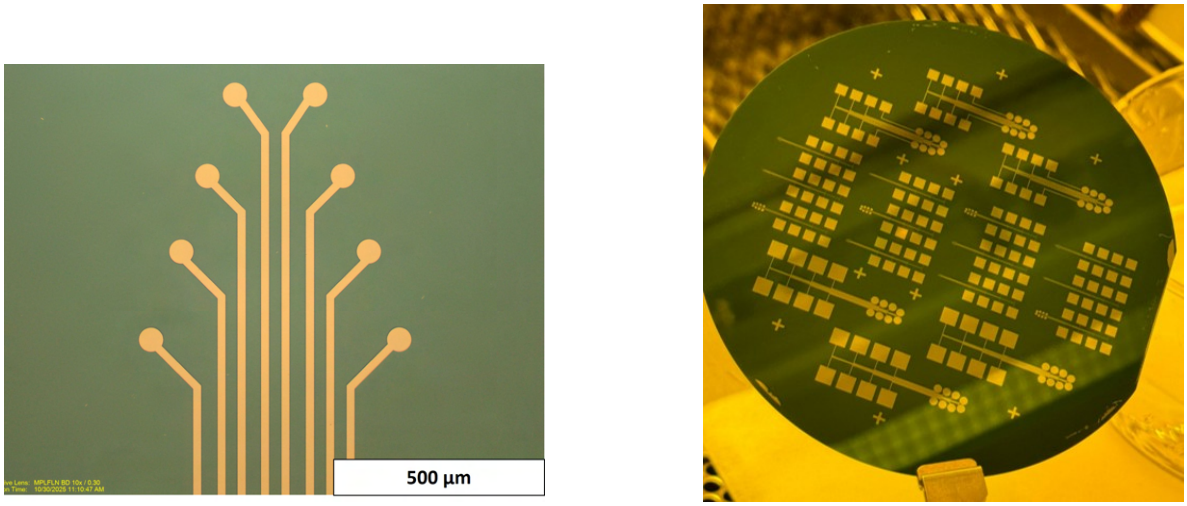

(a) (b)

Figure 2.5: Post lift-off image of the patterned gold electrodes.

edge-bead removal and backside cleaning were performed to ensure uniform film coverage across the wafer. The coated wafers were subsequently cured in a nitrogen-purged convection oven using a controlled thermal profile consisting of a 2 h ramp from room temperature to 250 $^{\circ}C$, a 1 h soak at 250 $^{\circ}C$, and a 2 h cool-down to room temperature. The cured BCB thickness was $\sim$2.5–3 μm [34, 35].

BCB was chosen as the passivation material due to its excellent chemical resistance, particularly to acidic and oxidative environments, low moisture absorption, and strong mechanical stability [34]. These properties are necessary, as the electrodes are subjected to repeated electrochemical cleaning and prolonged experiments in complex biological environments, as discussed in later chapters. In addition, BCB is widely used in neural and bioelectronic microdevices and is compatible with future scaling toward flexible or ultrathin microelectrode array platforms, enabling potential extension of this fabrication approach to mechanically compliant MEAs for in vivo spatial sensing applications [34, 35, 36].

Opening of the electrode sensing sites and contact pads was done through selective

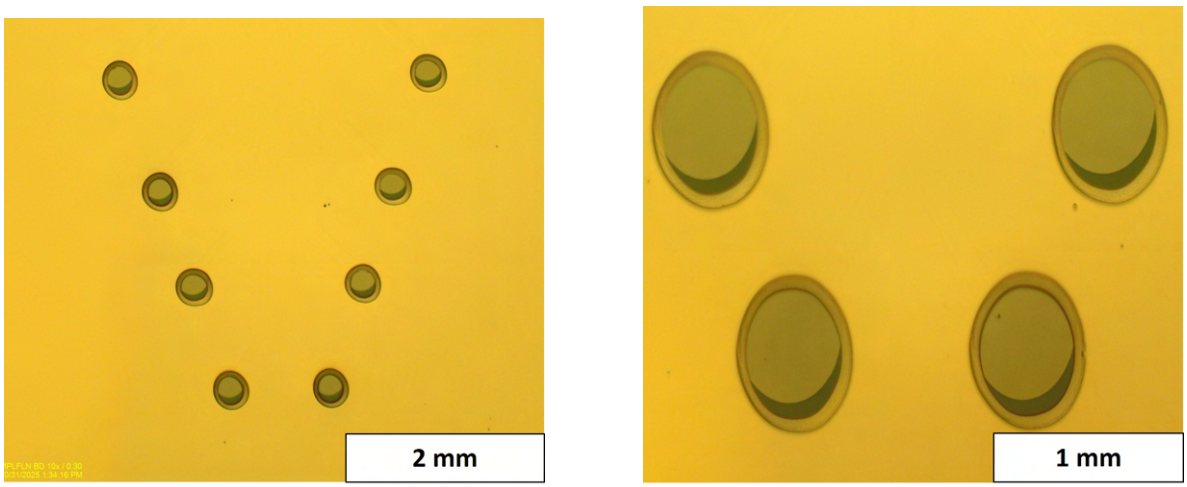

(a) (b)

Figure 2.6: Post-second exposure image of the patterned electrode sensing site and contact.

etching of the BCB passivation layer and the underlying chromium. For BCB etching, a 120 nm aluminium hard mask was first deposited by electron-beam evaporation. A second photolithography step, identical to the first lithography process, was then performed to pattern the sensing site and contact pad openings. Fig. 2.6 shows the post-lithography electrode sensing sites and contact pads. After lithography, the aluminium hard mask was etched using Aluminum Etchant Type A at an etch rate of approximately 80 nm/min for ∼2–3 min [37]. The exposed BCB was then etched using inductively coupled plasma reactive ion etching (ICP-RIE) using a CF_4/O_2 plasma, performed for 4 min 14 s, corresponding to an etch rate of 588.97 nm/min, resulting in complete removal of the cured BCB layer [38, 39]. Finally, the top chromium layer was removed using Chromium Etchant 1020, which has a etch rate of ∼50 nm/min, and was etched for approximately 1–2 min, thereby exposing the gold electrode sensing sites while leaving the surrounding regions fully passivated [40].

Fig. 2.7(a) shows post etch microscopic images of $1500\mu m$ and $500\mu m$ electrode sensing sites. The image corresponding to the 500 μm electrode design indicates a

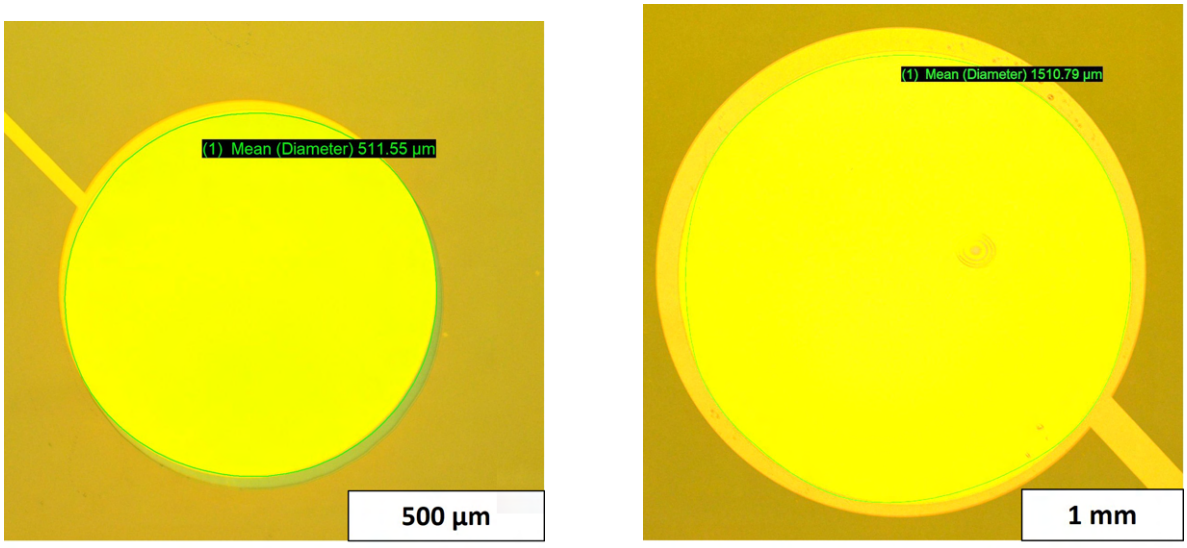

(a) (b)

Figure 2.7: Post-etch image of exposed gold electrode sensing sites following BCB and chromium etching, showing measured mean diameters for the (a) 500 μm design and (b) 1500 μm design.

measured mean diameter of approximately 511.6 μm, confirming close agreement with the intended design value. Similarly, 1500 μm design, shown in Fig. 2.7(b), yields a measured mean diameter of approximately 1510.8 μm. These images confirm accurate lithographic alignment between the second patterning step and the underlying metallization, as well as successful removal of the passivation and adhesion layers, resulting in well-defined, circular gold sensing sites.

2.2.2.2 Silicon Micromachining for Microelectrode Array Release

After completion of metallization and passivation, additional micromachining steps were required to define the final device geometry and enable physical release of the microelectrode arrays from the silicon substrate, as described in the following section. The Fig. 2.8 shows a schematic illustration of the process flow done to release the MEAs from the wafer.

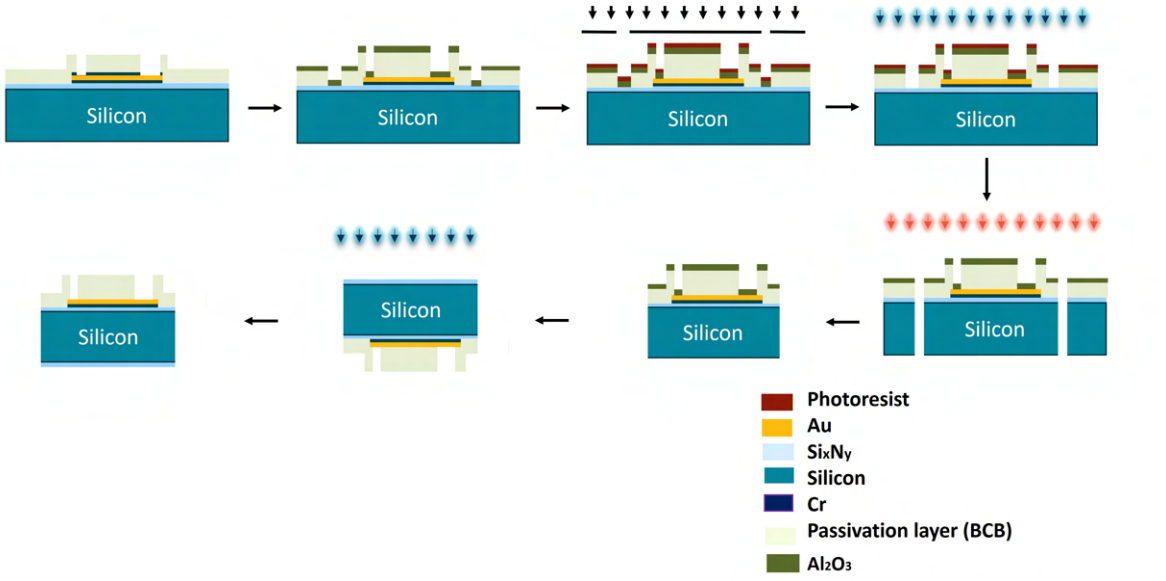

Figure 2.8: Schematic illustration of the microfabrication process flow for electrode release from the wafer.

Aluminium oxide (Al_2O_3) was used as the hard mask due to its high etch selectivity with respect to silicon during fluorine-based deep reactive ion etching (DRIE) processes. In Bosch-type silicon etching chemistries, Al_2O_3 exhibits a substantially lower etch rate than silicon, enabling it to function as a durable dielectric hard mask during prolonged plasma exposure and deep silicon micromachining steps [31, 41].

Al_2O_3 was deposited by reactive sputtering using an aluminium target in an Ar/O_2 ambient, employing a pulsed DC sputtering process. Deposition was carried out at a power of 300 W, with the chamber pressure maintained at approximately 3 mTorr and an Ar/O_2 flow ratio of 45/5 sccm. Pulsed DC sputtering was selected to promote the formation of dense, low pinholes oxide films with improved adhesion and plasma resistance compared to conventional DC sputtering [42]. Under these conditions, the deposition rate was $\sim$ 9.2 nm/min, and the deposition time was $\sim$ 21 min 44 s to obtain an Al_2O_3 film thickness of 200 nm.

Photolithography was used to define the microelectrode array (MEA) boundary

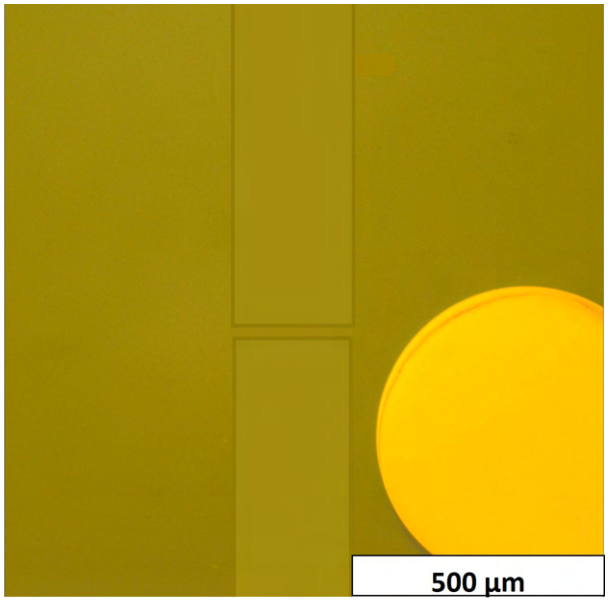

Figure 2.9: Post third lithography image of the patterned MEA boundary and silicon bridge structures used to define the device release trenches.

required for device release. The post-exposure microscopic image is shown in Fig. 2.9. The photolithography process employed for this step was identical to that used in the first and second lithography steps, including resist coating, exposure conditions, and development parameters.

The patterning was designed to include narrow silicon bridges that mechanically supported the devices during processing. The side trenches were defined with a width of 200 μm along the electrode boundary, while silicon bridges with widths of 20 μm and lengths of 200 μm were retained. These bridges were designed to facilitate easier handling of the wafer during deep silicon etching and subsequent processing. Final device release was achieved by mechanically breaking the bridges after completion of the remaining fabrication steps described later in this section.

Al_2O_3 etching was performed using ICP-RIE with a BCl_3 - based plasma chemistry. The Al_2O_3 film was etched at a rate of 40 nm/min and processed for $\sim$ 5 min 20 s, including overetch to ensure complete removal in the exposed regions[38].

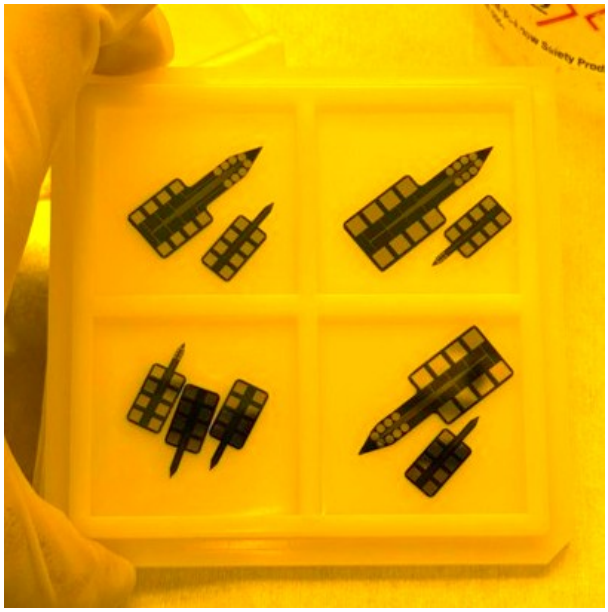

Figure 2.10: Image of the microelectrode arrays after DSE and mechanical release from the substrate.

Following Al_2O_3 removal, the BCB passivation layer was etched using a CF_4/O_2 plasma for approximately 4 min 20 s, opening the underlying Si_xN_y dielectric layer. Due to the high etch selectivity of Al_2O_3 relative to BCB, an additional aluminum hard mask was not required for this BCB etch step, unlike in earlier process stages [38, 39].

On the wafer backside, a 120 nm thin layer of aluminium was deposited and used as an etch stop for the deep silicon etching (DSE) process, protecting the underlying layers during through-wafer micromachining.

DSE was performed using a Bosch deep reactive ion etching (DRIE) process[43]. The process was performed by sequential application of SF_6 (for etching silicon) and C_4H_8 (for the formation of passivation layer) in a cycle to enable anisotropic removal of silicon while maintaining vertical sidewalls. This cyclic process was used to etch through the silicon substrate. The etch was carried out for $\sim$ 430 Bosch cycles.

Following completion of the deep silicon etch, the Al layer deposited on the wafer backside was removed using Aluminum Etchant Type A, consistent with the Al etch

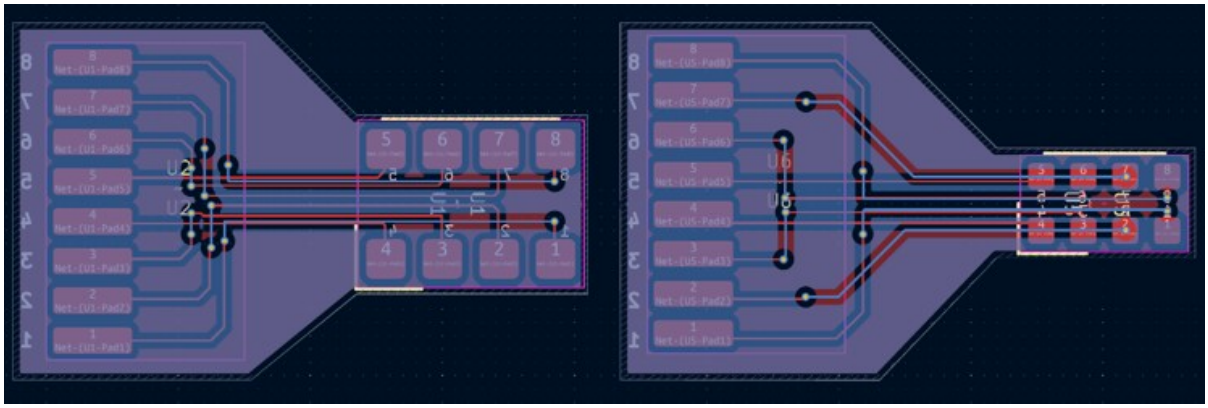

(a)

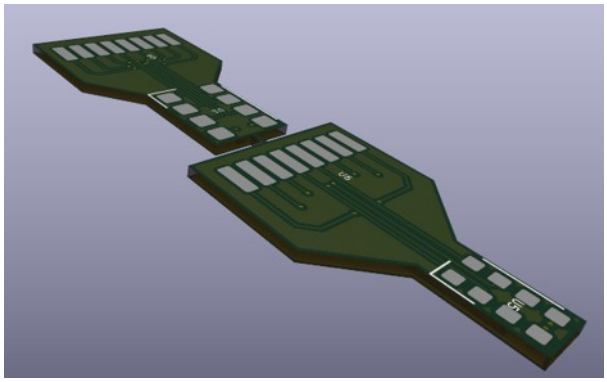

(b)

Figure 2.11: PCB interface design for MEA electrical interfacing. (a) KiCad PCB layout showing routing from MEA contact pads to external interface pads. (b) 3D PCB view.

procedure used in earlier fabrication steps[43]. To electrically isolate exposed silicon surfaces and provide mechanical protection to the released structures, a 200 nm silicon nitride (Si_xN_y) layer was deposited PECVD. Subsequently, residual Al_2O_3 on the front side was removed using ICP-RIE, following the same etch methodology described in earlier sections. Finally, the MEAs were released from the substrate using a scribing tool. The fully released devices are shown in Fig. 2.10.

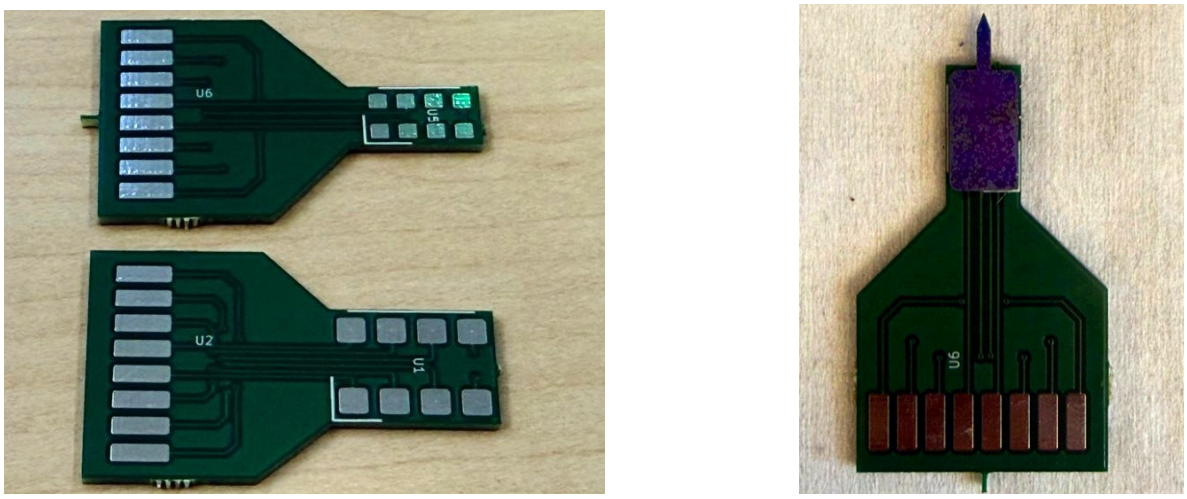

(a) (b)

Figure 2.12: Fabricated PCB interface and assembled MEA–PCB integration. (a) Fabricated custom PCBs corresponding to the two MEA designs. (b) MEA mounted on the PCB.

2.3 Custom PCB Interface for MEA Electrical Interfacing

A custom printed circuit board (PCB) was designed and fabricated to provide a reliable electrical interface between the microelectrode array (MEA) contact pads and external instrumentation. The PCB was designed using KiCad and had overall dimensions of 89.5 mm × 27 mm × 1.6 mm (length × width × thickness).

The PCB layout was designed to align with the eight contact pads of the MEA, enabling straightforward electrical routing from the microfabricated electrodes to external connectors. Fig. 2.11(a) and 2.11(b) show the PCB layout and 3D view generated during the design stage and Fig. 2.12(a) shows the image of the fabricated PCBs.

Electrical attachment between the MEA and the PCB was achieved by soldering the MEA contact pads directly onto the PCB pads using solder paste. This approach provided a mechanically stable and low-resistance electrical connection, suitable for repeated

electrochemical measurements. Figure 2.12(b) shows an image of the MEA mounted onto the custom PCB, illustrating successful alignment and electrical interfacing.

This custom PCB interface enabled robust handling of the MEAs during benchtop electrochemical testing and provided a practical platform for connection to potentiostats and external measurement electronics.

Chapter 3

Electrochemical Aptamer-Based Sensing and Data Analysis

3.1 Target Antibiotics and Aptamer Recognition

Electrochemical aptamer-based (EAB) sensors detect target molecules through selective binding to surface-confined nucleic acid aptamers. This molecular recognition is converted into a measurable electrochemical signal through binding-induced changes in electron-transfer kinetics [44, 45, 46, 47, 48]. In this work, polymyxin B was selected as the target antibiotic due to its clinical importance, narrow therapeutic window, and the need for real-time monitoring in biological fluids [49], [50].

Polymyxin B is a cyclic, cationic polypeptide antibiotic used for the treatment of multidrug-resistant Gram-negative bacterial infections [49], [50]. Despite its clinical utility, polymyxin B exhibits a narrow therapeutic window and is associated with dose-dependent nephrotoxicity and neurotoxicity, necessitating careful control of systemic drug concentration [49, 50, 51]. Due to these pharmacological characteristics, polymyxin B represents a clinically relevant target for pharmacokinetic monitoring using electrochemical

sensing platforms. Real-time or near-real-time measurement of polymyxin B concentrations could enable improved dosing strategies while reducing the risk of adverse effects.

Due to these pharmacological characteristics, polymyxin B represents a relevant target for pharmacokinetic monitoring using electrochemical sensing platforms. Real-time or near–real-time measurement of polymyxin B concentrations could enable improved dosing strategies and reduce the risk of adverse effects.

In this work, aptamers were synthesized with a thiol modification at the 5′ terminus to enable immobilization onto gold electrodes via gold–thiol chemistry. A methylene blue redox reporter was conjugated to the 3′ terminus of each aptamer to facilitate electrochemical transduction. This modification of the aptamer allows target binding to be detected through binding-induced changes in electron-transfer kinetics rather than through changes in equilibrium binding alone [44, 47, 52, 53].

The aptamer sequences and terminal modifications used in this study are -

```
5'-/5ThioMC6-D/ACGACGCCATACGGACAGTGCTAAGGTACCTTTCGT/3MB/-3'
```

*MB = Methylene Blue

Detailed procedures for aptamer preparation, electrode functionalization, and surface conditioning are described in Section 3.4.

3.2 Electrochemical Measurement Techniques

EAB sensors rely on changes in electron-transfer kinetics that arise from target-induced conformational change of surface-immobilized, redox-labeled aptamers. In this work, electrochemical measurements were performed using a three-electrode configuration and a combination of cyclic voltammetry (CV), square-wave voltammetry (SWV), and chronoamperometric cycling for electrode cleaning and roughening. Each technique serves

a distinct role in sensor preparation, characterization, and signal transduction. All electrochemical measurements were carried out using a conventional three-electrode configuration consisting of a gold working electrode (WE), a silver/silver chloride ($Ag|AgCl$) reference electrode (RE), and a platinum counter electrode (CE) [45]. The working electrode serves as the site of electron transfer between the redox-labeled aptamer and the electrode surface. The reference electrode provides a stable potential against which the working electrode is biased, while the counter electrode supplies the current required to maintain charge balance within the electrochemical cell during measurements [45].

3.2.1 Cyclic Voltammetry

Cyclic voltammetry is used to assess electrode cleanliness, electrochemical activity, and stability prior to and following surface modification. CV measurements were performed before and after functionalizing the working electrodes. Pre-functionalization CVs were recorded in $0.5M H_2SO_4$, as shown in Figure 3.1(a). Well-defined and stable voltammograms indicate there is an effective removal of organic contaminants and oxide layers, while any deviations in baseline current or the presence of hysteresis would indicate surface fouling or incomplete cleaning [45, 54].

After PolymyxinB aptamer immobilization and self-assembled monolayer formation on the electrodes, CV measurements were done in phosphate-buffered saline (PBS) at $37°C$ as shown in Figure 3.1(b). This confirms successful formation of the aptamer/self-assembled monolayer, which is shown as an increase in capacitive current and attenuation of surface redox features due to partial blocking of the gold surface [45], [55], [56].

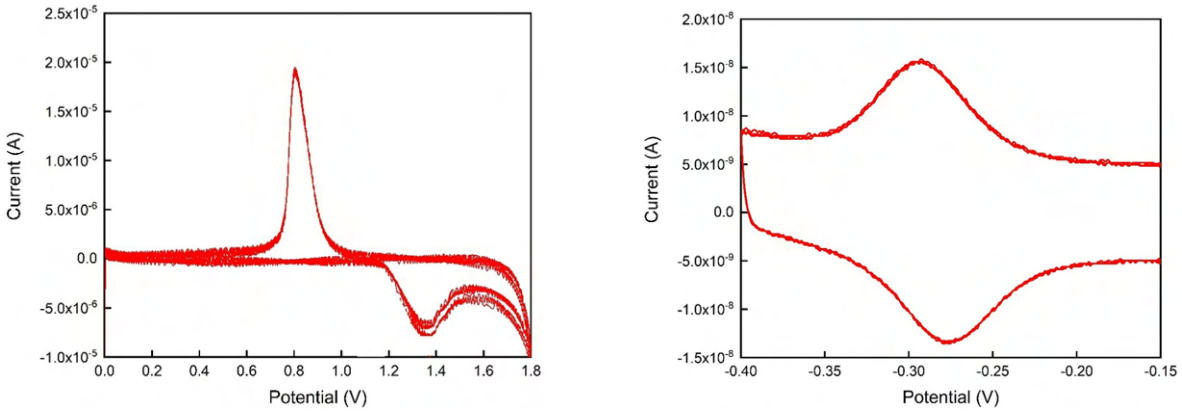

(a) (b)

Figure 3.1: CV scan in 0.5 M H_2SO_4 showing effective electrochemical cleaning and a stable gold surface prior to functionalization. (b) CV of an aptamer-functionalized working electrode recorded in PBS at 37°C.

3.2.2 Chronoamperometry

Electrochemical roughening was performed on gold wire control electrodes using chronoamperometric potential pulsing in $0.5M H_2SO_4$. The electrode potential was stepped to 2.2 V versus $Ag|AgCl$ with a pulse width of 20 ms, and this was repeated for a total of 100 roughening cycles. This treatment induces controlled surface restructuring, increasing the electrochemically active surface area[54, 57, 58, 59, 60].

Electrochemical roughening of gold electrodes has previously been shown to enhance signal gain in EAB sensors by increasing redox reporter accessibility and reducing steric crowding within the self-assembled monolayer [54, 57, 58]. In this work, CV measurement was done to evaluate changes in electrochemically active surface area before and after roughening.

CV measurements recorded for planar gold electrodes of diameters 1500 μm and 500 μm and for an unroughened gold wire control electrode are shown in Figure 3.2(a). The magnitude of the gold oxide reduction peak scales with electrode geometry, confirming that the CV response reflects the physical surface area of the electrodes.

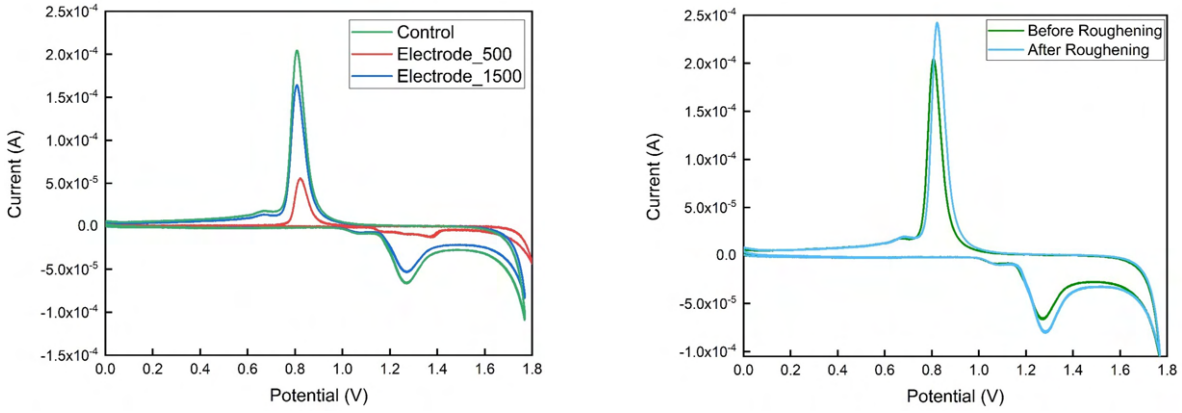

(a) (b)

Figure 3.2: CV measurements recorded in 0.5M H_2SO_4 of (a) unroughened planar gold electrodes (1500μm and 500μm diameter) and an unroughened gold wire control electrode to assess differences in physical surface area, and (b) a gold wire control electrode before and after electrochemical roughening.

Cyclic voltammograms acquired before and after electrochemical roughening of the gold wire control electrode are shown in Figure 3.2(b). After roughening, the electrode shows an increase in both the gold oxide reduction peak current and the capacitive background current relative to the unroughened control. This behavior is consistent with an increase in electrochemically active surface area induced by the chronoamperometric roughening method.

The charge associated with this reduction peak was obtained by integrating the corresponding current, and the electrochemically active surface area was calculated by dividing the measured charge by a charge density of 400 μCcm^{-2}, corresponding to a complete monolayer of chemisorbed oxygen on gold [45, 62].

3.2.3 Square-Wave Voltammetry

Square-wave voltammetry is used for EAB sensing measurements and kinetic differential measurements. SWV enhances sensitivity to faradaic electron transfer while

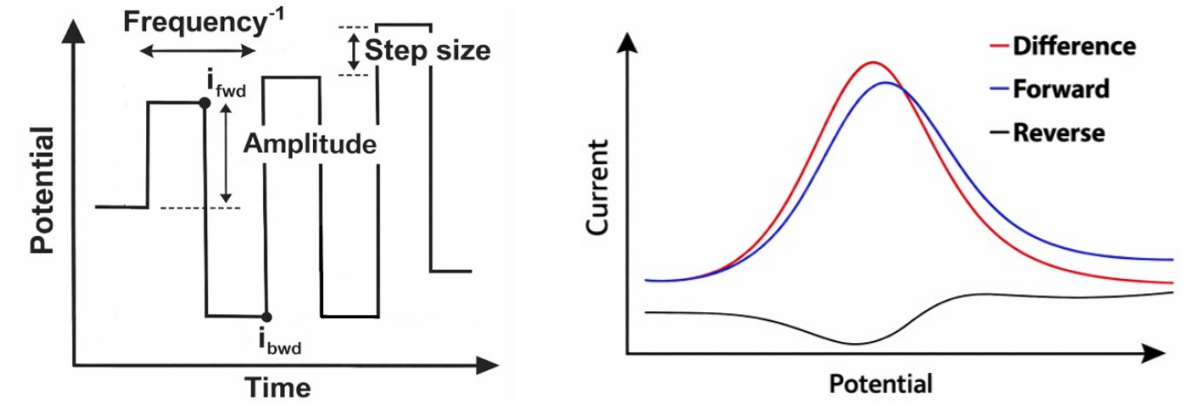

(a) (b)

Figure 3.3: Principle of square-wave voltammetry (SWV). (a) Schematic of the applied SWV potential waveform, consisting of a staircase base potential with a superimposed symmetric square-wave modulation. The forward and reverse currents i_{fwd} and i_{bwd} are sampled at the end of each pulse, with the waveform defined by the step size, amplitude, and square-wave frequency[10]. (b) Schematic showing square wave voltammogram [61] .

minimizing non-faradaic background currents, making it well-suited for surface-confined redox systems [45, 63, 64].

In SWV, a rising staircase potential is superimposed with a square-wave modulation, and the faradic current is sampled at the end of forward and reverse pulse (i_{fwd} and i_{bwd}). The difference between these sampled currents is plotted as a function of potential to generate the voltammogram. Because current is measured after capacitive charging has largely decayed, this differential sampling suppresses non-Faradaic background while enhancing sensitivity to kinetically limited electron-transfer processes. SWV demonstrated in Fig. 3.3. As a result, the square-wave frequency can be tuned to selectively emphasize electron-transfer rates relevant to electrochemical DNA and aptamer-based sensors, providing a powerful means of optimizing signal gain and selectivity[10, 61].

Because electron transfer in EAB sensors is kinetically limited, the measured response is strongly dependent on square-wave frequency [44, 63, 65, 66]. At lower frequencies, the influence of slower electron-transfer kinetics results in reduced peak currents whereas at

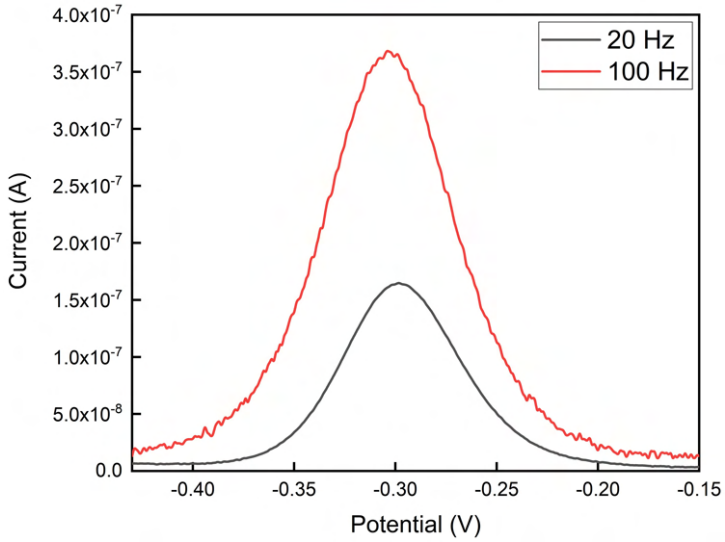

Figure 3.4: SWV measurements recorded at 20 Hz and 100 Hz from polymyxin B aptamer-functionalized electrodes in PBS at 37 °C, showing the frequency dependence of the EAB sensor response.

higher frequencies, the measured signal is dominated by faster electron-transfer processes, resulting in higher peak currents as shown in Fig. 3.4. The SWV shown in the aforesaid figure were obtained from electrodes functionalized with the polymyxin B aptamer and measured in PBS at 37°C.

Target binding alters the conformational dynamics of the aptamer, resulting in frequency-dependent modulation of the SWV signal. This behaviour forms the basis for kinetic differential measurement strategies used throughout this work [65, 66, 67].

Together, CV, electrochemical roughening, and SWV provide a framework for electrode characterization, surface conditioning, and kinetic interrogation of EAB sensors. These techniques support frequency-dependent analysis and enable quantitative comparison of sensor performance across electrode geometries, surface morphologies, and measurement environments.

3.3 Frequency Dependence and Kinetic Differential Measurement (KDM)

In EAB sensors, signals obtained using SWV exhibit a strong dependence on square-wave frequency due to kinetically limited electron transfer between the redox reporter and the electrode surface.

In addition to improving sensitivity, the strong dependence of EAB sensor gain on square-wave frequency helps in removal of signal drift that can arise during prolonged measurements, particularly in complex biological environments. Such drift may originate from surface fouling, gradual changes at the electrode–electrolyte interface, or nonspecific adsorption, and often manifests as slow variations in absolute signal magnitude [65], [68], [69]. Exploiting frequency-dependent signal behavior therefore provides a practical framework for drift correction in EAB sensing.

3.3.1 Signal-On and Signal-Off Frequencies

For EAB sensors, target binding does not uniformly scale the SWV response across all frequencies. Instead, binding-induced changes in electron-transfer kinetics can result in an increase in signal at certain frequencies and a decrease at others. Frequencies at which target binding produces an increase in signal are referred to as signal-on frequencies, whereas frequencies at which binding produces a decrease in peak current are referred to as signal-off frequencies. Fig. 3.5 shows how the SWV responses in the absence of target and in the presence of target at both signal-on and signal-off frequencies.

The specific signal-on and signal-off frequencies depend on factors including aptamer structure, surface chemistry, and electrode morphology, and must therefore be identified experimentally which is done in the later section based on the aptamer [63, 65, 69].

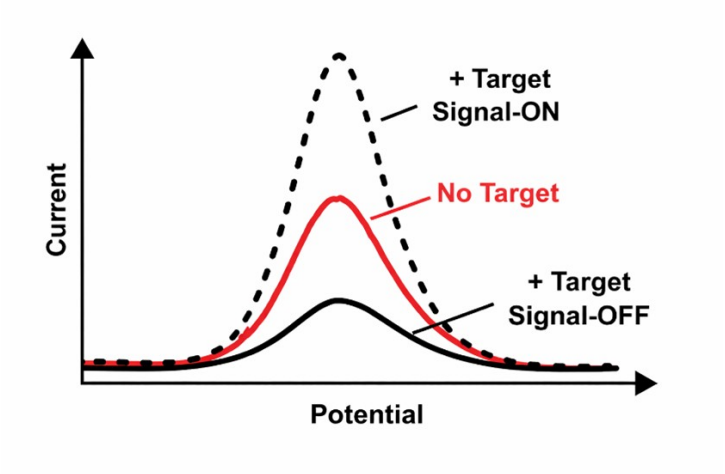

Figure 3.5: Schematic illustration of signal-on and signal-off behavior in electrochemical aptamer-based sensors. Target binding produces an increase in SWV peak current at signal-on frequencies and a decrease in peak current at signal-off frequencies relative to the no-target condition.[10]

Although the absolute signals at these frequencies may drift over time, particularly in complex biological environments, this drift is often correlated across frequencies. This correlated behavior enables the use of differential measurement strategies, such as kinetic differential measurement (KDM), to suppress drift while preserving sensitivity to target binding.

3.3.2 Kinetic Differential Measurement Definition

To suppress common-mode drift and reduce sensitivity to variations in absolute signal magnitude, a kinetic differential measurement (KDM) parameter was used. The fractional signal change at a given square-wave frequency f is defined as -

$$i(f) = \frac{I(f, target) - I(f, 0)}{If(0)}$$

where $I(f, target)$ and $I(f, 0)$denote the square-wave voltammetric peak currents measured in the presence and absence of target, respectively

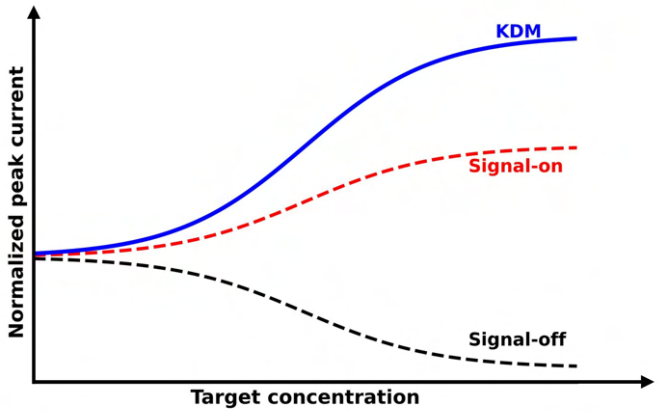

Figure 3.6: Schematic illustration of kinetic differential measurement (KDM) in electrochemical aptamer-based sensors.[62]

The kinetic differential measurement (KDM) was then calculated as

$$KDM = i(f_{on}) - i(f_{off})$$

where f_{on} and f_{off} correspond to square-wave frequencies at which target binding produces, respectively, a large and minimal change in signal. Although both frequencies are subject to identical environmental perturbations (common-mode drift), their differential response to the analyte allows for the subtraction of background noise while preserving the integrity of the target-induced signal. This principle is illustrated schematically in Fig. 3.6.

This normalization reduces sensitivity to changes in electrode surface area, baseline drift, and nonspecific environmental effects that similarly affect both frequencies. As a result, the KDM metric enhances sensitivity to binding-induced changes in electron-transfer kinetics while improving measurement stability in complex media [66], [63], [69].

The use of KDM enables direct comparison of sensor performance across different electrode geometries and surface conditions, including planar microelectrode array electrodes

and gold wire control electrodes, as well as roughened and unroughened surfaces. Because KDM is dimensionless and normalized, it facilitates statistical analysis and comparison across experiments without requiring absolute current matching.

KDM-based analysis has previously been shown to improve robustness and reduce drift in EAB sensor measurements, particularly under prolonged interrogation and in complex biological matrices [65, 66, 67]. Accordingly, KDM was used throughout this work as the primary parameter for evaluating sensor response and comparing performance across electrode platforms.

3.4 Functionalization of Electrodes

This section describes the procedures used for aptamer preparation, electrode cleaning, and surface functionalization. These steps were applied for all electrode geometries to ensure reproducible surface chemistry before experiments.

3.4.1 Electrode Electrochemical Cleaning and Roughening

This process was done prior to aptamer functionalization to ensure clean gold surface conditions. All electrochemical procedures were carried out using a three-electrode configuration consisting of the gold working electrode, a platinum counter electrode, and an $Ag|AgCl$ reference electrode. Working electrodes included planar gold microelectrodes with diameters of 1500 μm and 500 μm, as well as PTFE-wrapped gold wire control electrodes with 3 mm exposed length and 200 μm diameter. Electrodes were secured in a shot glass electrochemical cell using tape for stable positioning during measurements.

Electrochemical cleaning was first performed in $0.5M$ NaOH by repeated cyclic voltammetry scans between $1.0V$ and $2.0V$ (all potentials versus $Ag|AgCl$) at a scan rate of $1Vs^{-1}$ for 320 cycles using a CHI1040C multipotentiostat (CH Instruments, Inc.).

Following cleaning, electrodes were rinsed thoroughly with deionized water and transferred to $0.5MH_2SO_4$, where four CV were recorded between $0.0V$ and $1.8V$ at a scan rate of $0.1Vs^{-1}$ to confirm surface cleanliness.

After this step, planar microelectrodes and a subset of control gold wires were removed and reserved as unroughened electrodes. The remaining control gold wire electrodes were electrochemically roughened in $0.5MH_2SO_4$ using chronoamperometric potential pulsing. The electrode potential was alternated between an initial potential of $0.0V$ and a high potential of $2.0V$ (versus $Ag|AgCl$) for a total of 100 roughening cycles. Each pulse had a duration of 20 ms with no quiet time between pulses. This treatment was used to increase the electrochemically active surface area of the gold wire control electrodes prior to functionalization [65].

3.4.2 Electrode Functionalization

DNA aptamers modified with a 6-carbon thiol linker at the $5'$ terminus and methylene blue at the $3'$ terminus were used for sensor functionalization. Aptamer stock solutions were stored at $-20°C$ until use. Because the thiol groups were provided in oxidized disulfide-protected form, aptamer solutions were reduced prior to immobilization to generate free thiol groups for gold–thiol attachment [47, 58, 64].

For reduction, a 2 μL aliquot of 100 μM aptamer was combined with 18 μL of tris(2-carboxyethyl) phosphine TCEP at a large molar excess and incubated for 1 h at room temperature in the dark. Following reduction, the aptamer solution was diluted with 380 μL of phosphate-buffered saline containing $2mM$ $MgCl_2$ to a final volume of 400 μL. Prepared aptamer solutions were used immediately to minimize thiol re-oxidation.

Freshly cleaned and roughened gold electrodes were immersed in the reduced aptamer solution and incubated for 1 h at room temperature in the dark to allow formation of a

self-assembled monolayer via gold–thiol bonding.

To passivate the remaining exposed gold surface and reduce nonspecific adsorption, aptamer-functionalized electrodes were subsequently backfilled with 6-mercapto-1-hexanol MCH solution. The MCH solution was prepared by diluting 1.37 μL of 6-mercapto-1-hexanol in 1 mL of PBS, corresponding to a concentration of approximately 10–20 mM. Electrodes were incubated in the MCH solution for 12–18 h at room temperature in the dark. Following backfilling, electrodes were rinsed thoroughly with deionized water and used for electrochemical measurements [70], [71].

3.5 Polymyxin B Sensing Results and Data Analysis

In this section, we discuss the electrochemical sensing performance of polymyxin B using EAB sensors functionalized on planar microelectrode arrays and gold wire control electrodes. The analysis focuses on frequency-dependent sensor response, KDM behavior, binding characteristics, and statistical comparison between electrode geometries and measurement environments.

3.5.1 CV Measurement After Functionalization

Cyclic voltammetry measurements performed after electrode functionalization in PBS and bovine blood (7 days old) at $37°C$, scanned at a rate: $50mVs^{-1}$ are shown in Fig. 3.7(a) and Fig. 3.7(b), respectively.

In PBS, all electrode types show clear faradaic current associated with the methylene blue redox reporter, with peak currents increasing from planar microelectrodes to unroughened and roughened gold wire controls. Roughened control electrodes show the highest peak currents, consistent with their increased electrochemically active surface area.

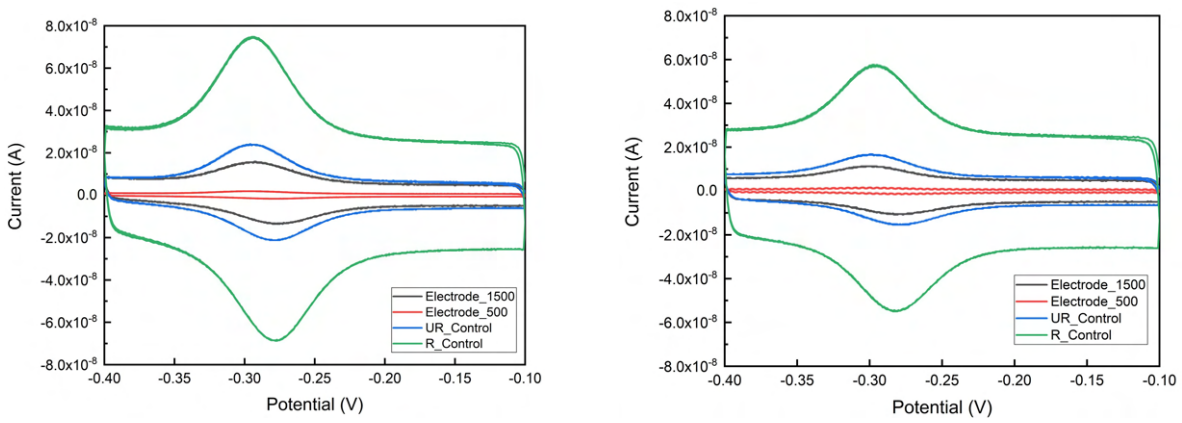

Figure 3.7: CV measurements for planar and control electrodes in (a) PBS at 37°C and (b) bovine blood at 37°C.

In bovine blood, the overall shapes are preserved, but with reduced faradic peak amplitudes and increased background currents across all electrodes relative to PBS. Despite this attenuation, distinct voltammogram shape is seen for all electrode types, indicating stable electrochemical behavior of the functionalized interfaces blood. The reduced peak currents observed in blood are due to increased solution resistance, nonspecific adsorption of blood components at the electrode interface, and partial attenuation of electron transfer due to protein fouling [65], [70], [71].

3.5.2 Frequency-Dependent Response and Identification of Signal-On and Signal-Off Frequencies

The frequency-dependent response of the polymyxin B sensors was done using square-wave voltammetry across a range of 10Hz-300Hz frequencies in both PBS and bovine blood at 37 °C, as shown in Fig. 3.8 and Fig. 3.9. For all electrode geometries, both the sign and magnitude of the signal change depended strongly on square-wave frequency, indicating kinetically limited electron-transfer behavior [44, 63, 65].

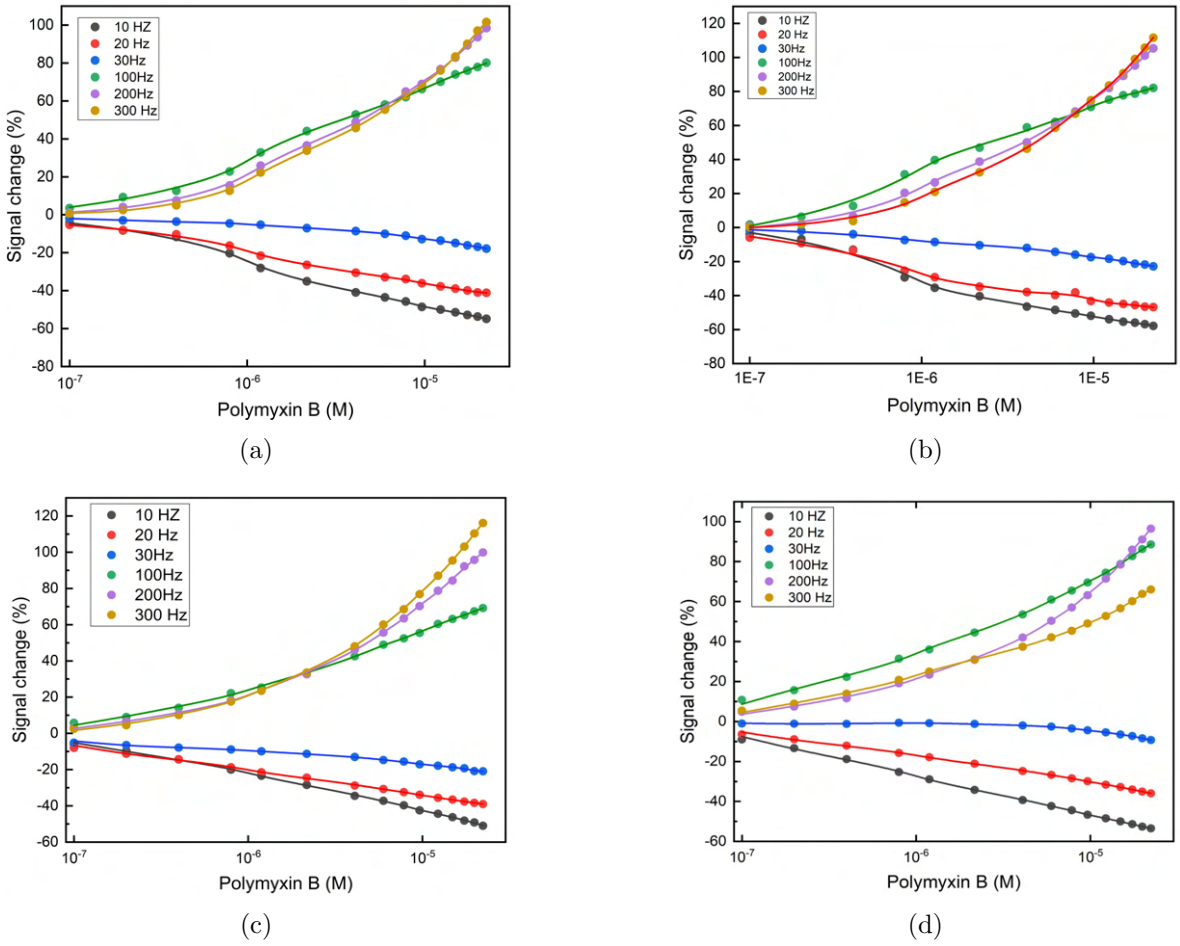

Figure 3.8: Frequency maps in PBS at 37 °C for (a) planar electrode of 1500 μm diameter, (b) planar electrode of 500 μm diameter, (c) unroughened control gold wire, and (d) roughened control gold wire.

At lower frequencies, i.e, 10 Hz and 20 Hz, increasing polymyxin B concentration produced a monotonic decrease in signal, whereas at higher frequencies, particularly 100 Hz and above, target binding resulted in a monotonic increase in signal. This qualitative behavior was observed across the planar microelectrodes and gold wire controls, both in PBS and bovine blood, despite differences in absolute signal magnitude. Based on these frequency maps, 20 Hz was selected as the signal-off frequency and 100 Hz as the signal-on frequency for subsequent KDM in both medium.

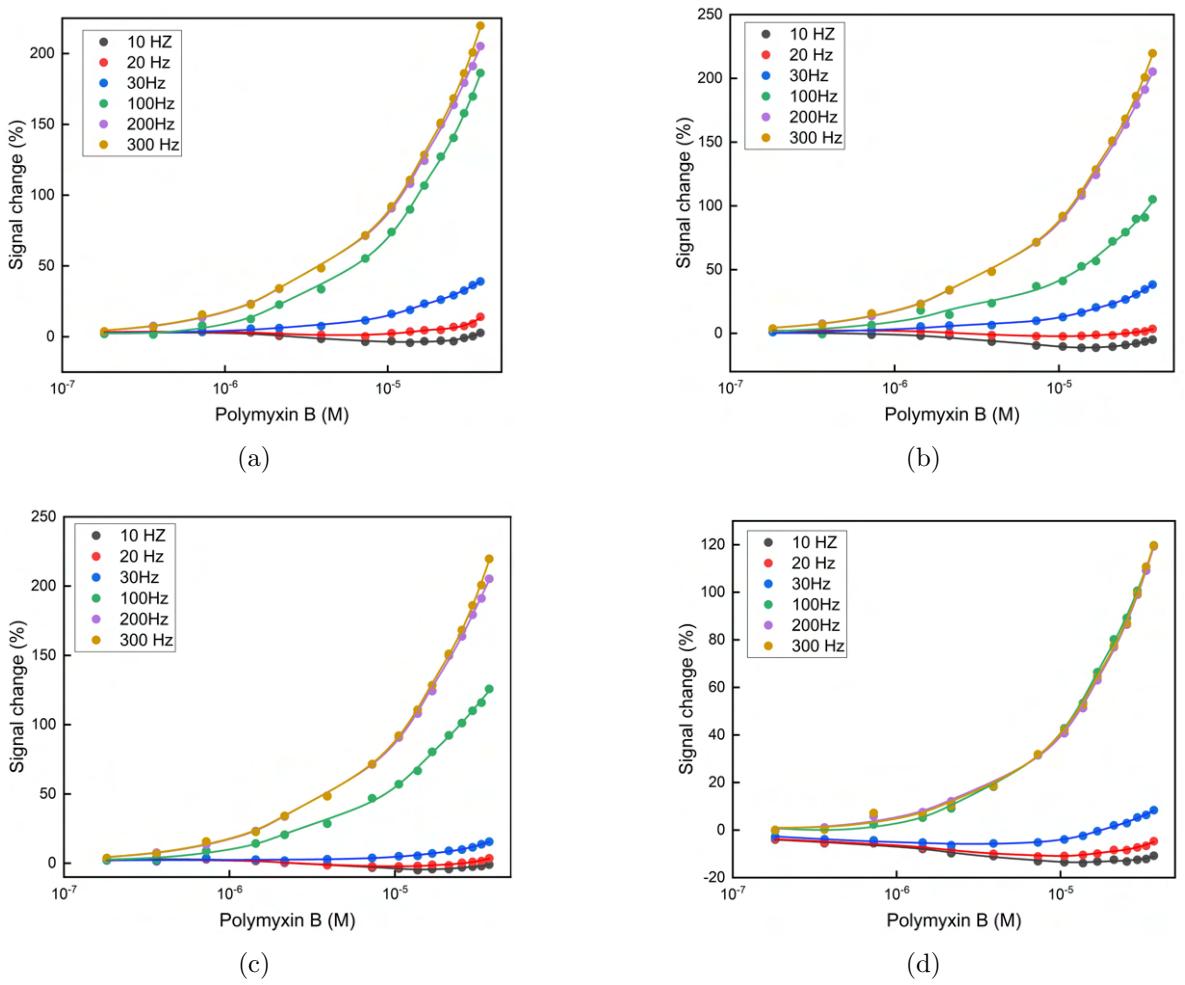

Figure 3.9: Frequency maps in bovine blood at 37 °C for (a) planar electrode of 1500 μm diameter, (b) planar electrode of 500 μm diameter, (c) unroughened control gold wire, and (d) roughened control gold wire.

3.5.3 SWV Response at Selected Signal-Off and Signal-On Frequencies

Square-wave voltammograms measured at the selected signal-off (20 Hz) and signal-on (100 Hz) frequencies in PBS and bovine blood at $37°C$ are shown in Fig.3.10 and 3.11. At 20 Hz, all electrode geometries exhibit reduced peak currents relative to 100 Hz, showing slower effective electron-transfer kinetics at off-frequency. However, at 100 Hz, the SWV

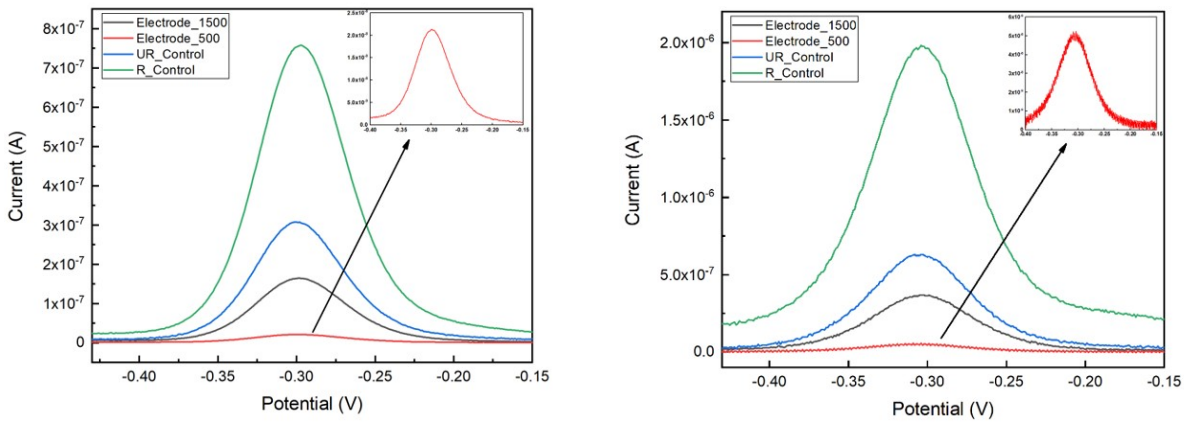

(a) (b)

Figure 3.10: SWV measurements in PBS at 37 °C : (a) 20 Hz square-wave frequency and (b) 100 Hz square-wave frequency. *The insets show the SWV response for planar electrode of 500 μm diameter*

response is enhanced across all electrodes, with roughened gold wire controls showing the largest peak currents, followed by unroughened controls and planar microelectrodes. For a given frequency, peak currents are lower in bovine blood than in PBS, reflecting increased background currents and partial attenuation of faradaic charge transfer in the complex biological environment [44, 63]. Despite this attenuation, the relative responses across electrode types and the frequency-dependent contrast between 20 Hz and 100 Hz are seen in both media.

3.5.4 Kinetic Differential Measurement (KDM) Analysis

For the Analysis, KDM was calculated using equation 1 to quantify polymyxinB binding. KDM Analysis was done across all electrode geometries in PBS and bovine blood at $37°C$ using 20 Hz - 100 Hz as frequency pair. The KDM response as a function of polymyxin B concentration are shown in Fig. 3.12(a) for PBS and Fig. 3.12b) for bovine blood.

In both media, the KDM signal increased monotonically with polymyxin B concentra-

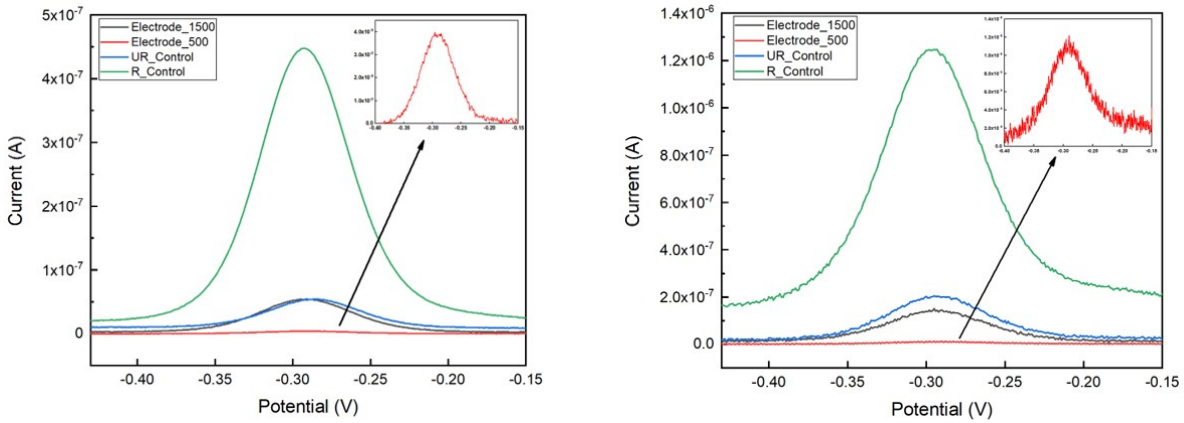

(a) (b)

Figure 3.11: SWV measurements in bovine blood at 37 °C : (a) 20 Hz square-wave frequency and (b) 100 Hz square-wave frequency. *The insets show the SWV response for planar electrode of 500 μm diameter*

tion and was well fitted by Langmuir Hill binding model[19]. The data analysis provided an estimate value of dissociation constants (K_D) and Hill coefficients n_h for each electrode geometry, with the values summarized in Table 3.1.

In PBS, all electrode types showed clear concentration-dependent responses, with planar microelectrodes exhibiting lower K_D values than gold wire controls. Hill coefficients were below unity, indicating mildly non-cooperative binding behavior typical of surface-confined aptamer systems. The high R^2 values obtained for all fits indicate that the Langmuir–Hill model accurately describes the KDM response in buffer.

In bovine blood, the KDM responses remained stable but give larger K_D values across all electrode geometries, indicating reduced apparent binding affinity. This shift reflects the influence of the complex blood environment, including nonspecific protein adsorption, increased ionic strength, and altered mass transport. Despite these effects, the Hill coefficients in blood remained close to unity for most electrode types, suggesting that the fundamental aptamer–target binding mechanism is preserved.

The increased K_D values in blood also indicate an important feature characteristic of

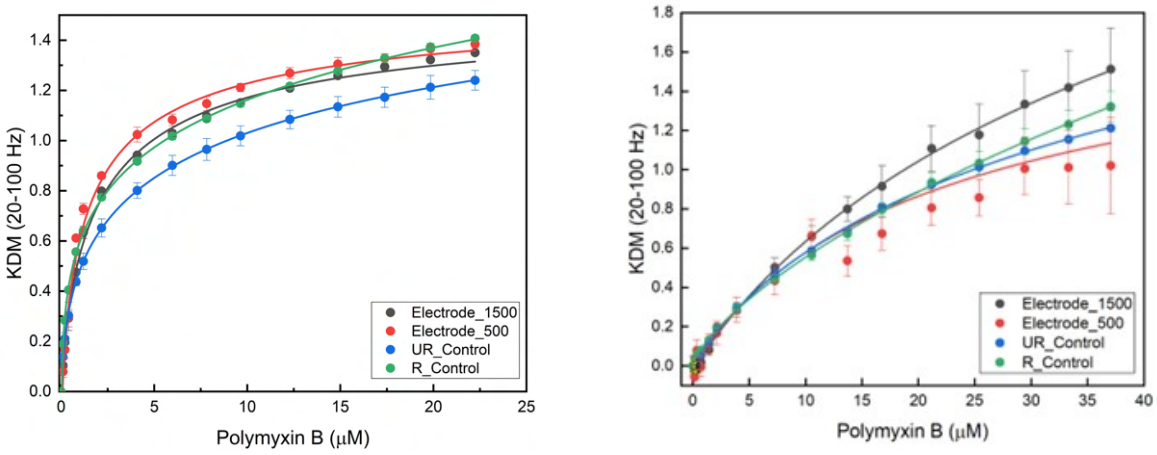

Figure 3.12: KDM response of polymyxin B EAB sensors using a 20-100 Hz frequency pair in (a) PBS at 37 °C and (b) bovine blood at 37 °C.

polymyxinB that it shows strong plasma protein binding. Approximately 90% or more of polymyxinB is protein-bound [51] meaning that only a small fraction of the total drug concentration is free and available for sensing. For example, a total concentration of 10 μM corresponds to a free concentration of at most $\sim 1 \mu M$. Because only free drug can be detected by electrochemical aptamer-based sensors, the effective concentration sensed in blood is substantially lower than in PBS, leading to a rightward shift in the KDM binding curves[49, 50, 51, 72, 73].

Overall, these results demonstrate that while biological matrix environment and protein binding reduce apparent binding affinity in blood, the KDM approach provides robust and interpretable binding metrics across electrode geometries and measurement environments.

3.5.5 Statistical Analysis of KDM Responses

While KDM responses show clear concentration-dependent trends, statistical analysis is required to understand how electrode geometries effect the KDM response. One-way

Table 3.1: Binding parameters extracted from fits in different media and electrode configurations.

Medium	**Electrode Dimension**	$\mathbf{K}_D$ **(**μ**M)**	$\mathbf{n}_H$	$\mathbf{R}^2$
PBS	1500 μm	2.26 ± 0.27	0.75 ± 0.05	0.99789
	500 μm	1.42 ± 0.21	0.85 ± 0.09	0.99340
	Unroughened Control	5.92 ± 0.68	0.58 ± 0.02	0.99966
	Roughened Control	8.42 ± 2.76	0.49 ± 0.03	0.99869
Bovine Blood	1500 μm	51.48 ± 20.92	0.90 ± 0.08	0.99861
	500 μm	24.51 ± 19.44	0.90 ± 0.23	0.96338
	Unroughened Control	42.19 ± 6.77	0.84 ± 0.03	0.99937
	Roughened Control	354.07 ± 15.60	0.74 ± 0.02	0.99973

analysis of variance (ANOVA) was used to test whether statistically significant differences exist in KDM responses across electrode types at each polymyxin B concentration. This analysis was performed separately for measurements obtained in PBS and bovine blood using the 20–100 Hz KDM response.

One-way ANOVA tests the null hypothesis that the mean KDM responses across all electrode groups are equal at a given concentration. The ANOVA F-statistic is defined as [74]

$$F = \frac{variance\,between\,groups}{variance\,within\,groups}$$

The p-value associated with the ANOVA F-statistic is calculated from the cumulative distribution function (CDF) of the F-distribution. The corresponding p-value represents the probability of observing the measured differences assuming the null hypothesis is true. A significance threshold of $p < 0.05$ was used, such that:

- $p < 0.05$ indicates statistically significant differences between electrode groups.
- $p \geq 0.05$ indicates no statistically detectable difference.

In PBS, the ANOVA show p-values below 0.05 at several intermediate polymyxin B concentrations shown in Fig. 3.13(a).This indicates that statistically significant differences

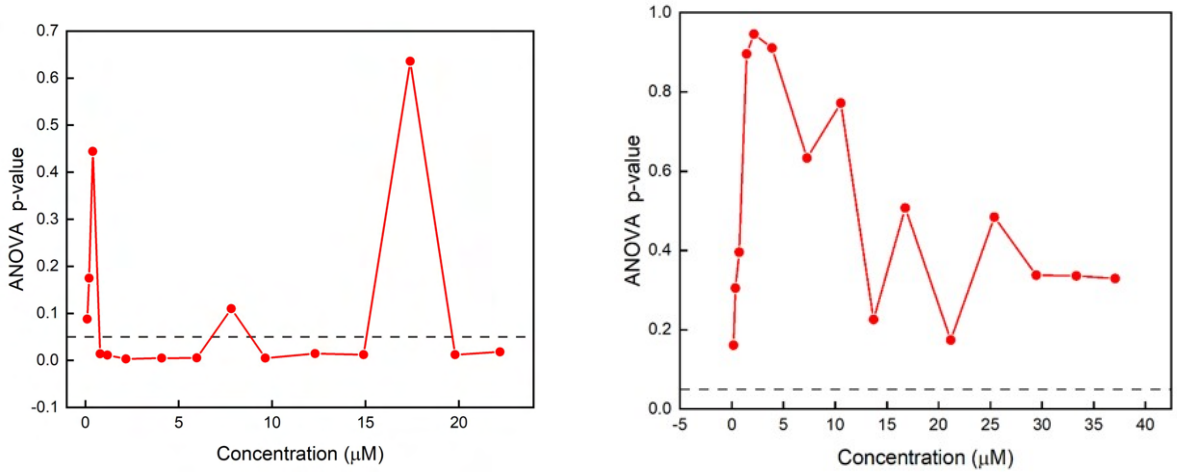

(a) (b)

Figure 3.13: One-way ANOVA p-values as a function of polymyxin B concentration for KDM responses measured in (a) PBS at 37 °C and (b) bovine blood at 37 °C. The dashed horizontal line denotes the significance threshold ($p = 0.05$).

in KDM responses across electrode geometries is present. At very low concentrations, signals are near baseline and differences are difficult to resolve, while at high concentrations the responses approach saturation, leading again to higher p-values. Overall, the PBS results demonstrate that electrode geometry significantly influences KDM response under controlled buffer conditions.

While in bovine blood, p-values greater are than 0.05 across most of the tested concentration range, as shown in Fig. 3.13(b). This indicates that differences between electrode geometries are not statistically significant in blood. The increased variability in blood measurements is due to the biological effects, including nonspecific protein adsorption, higher background noise, and reduced free drug availability, which collectively mask geometry-dependent differences observed in PBS.

Pairwise comparisons were performed using the Tukey honestly significant difference (HSD) post-hoc test to identify which electrode pairs shows most statistically significant differences in PBS. The results of this analysis are summarized in Table 3.2, where

statistically significant comparisons ($p < 0.05$ are highlighted [75]. The analysis reveals statistically significant differences ($p < 0.05$) primarily between planar microelectrodes and gold wire control electrodes over a limited concentration range. The 1500 μm planar electrodes and the roughened gold wire controls do not have p-values below 0.05 across the tested concentration range. This indicates that the KDM response of the 1500 μm planar electrodes is statistically indistinguishable from that of the roughened control electrodes in PBS.

Table 3.2: Pairwise statistical comparison across electrode configurations at different concentrations.

Concentration (μM)	1500 μm vs 500 μm	1500 μm vs UR	1500 μm vs R	500 μm vs UR	500 μm vs R	UR vs R
0.0999	0.9901	0.3661	0.14	0.2766	0.1074	0.7557
0.2	0.9962	0.781	0.2243	0.6758	0.1833	0.5501
0.399	0.9957	0.9906	0.4541	0.9999	0.5513	0.5841
0.796	**0.0216**	0.9229	0.663	**0.0146**	**0.0515**	0.3885
1.19	0.0721	0.123	0.6695	0.0092	**0.0290**	0.3768
2.17	0.052	**0.0245**	0.14	**0.0029**	**0.008**	0.2734
4.09	0.0559	**0.0468**	0.1996	**0.0044**	**0.0103**	0.4444
5.97	0.0746	**0.0399**	0.1939	**0.0047**	**0.0124**	0.3758
7.82	0.8786	0.2093	0.638	0.1056	0.3296	0.6551
9.64	0.0567	**0.041**	0.3661	**0.0041**	**0.0152**	0.2062
12.3	0.1618	0.0772	0.6074	**0.0114**	0.0521	0.2553
14.9	0.173	0.0533	0.7087	**0.0092**	0.065	0.1375
17.4	0.6609	0.9892	1.000	0.8095	0.6758	0.9920
19.8	0.1685	0.0548	0.9984	**0.0092**	0.1955	**0.0485**
22.2	0.3601	0.0612	0.9449	**0.0159**	0.5864	**0.0401**

3.5.6 Overnight Signal Drift in Bovine Blood at $37°C$

Long-term signal stability is a crucial requirement for EAB sensors intended for use in biological fluids, particularly for applications involving continuous or prolonged monitoring. To evaluate signal drift under physiologically relevant conditions, overnight measurements were performed in bovine blood at $37°C$ using planar microelectrodes and gold wire control electrodes.

Fig. 3.14 shows the relative change in signal over approximately 13 hours for three electrode types: 1500 μm planar microelectrodes, unroughened gold wire controls, and

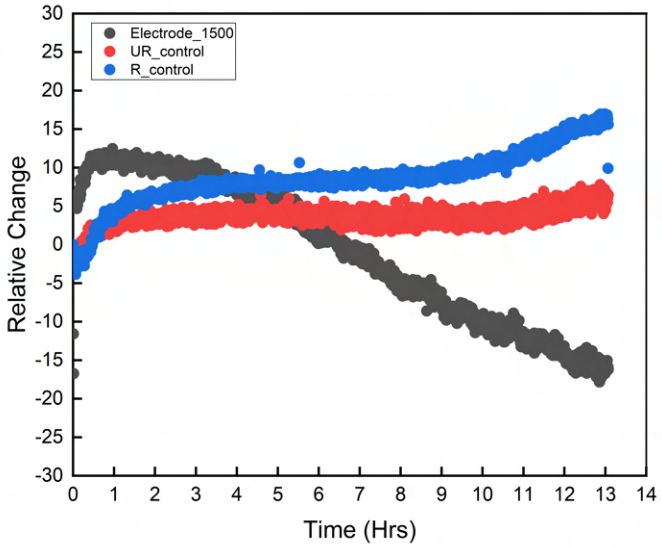

Figure 3.14: . Overnight signal drift of EAB sensors in bovine blood at $37°C$. Relative signal change is shown for 1500 μm planar microelectrodes, unroughened gold wire controls (UR), and roughened gold wire controls (R).

electrochemically roughened gold wire controls. The 500 μm planar microelectrodes are not shown due to excessive noise arising from their smaller electrochemically active surface area, which results in lower absolute faradaic currents and a reduced signal-to-noise ratio during prolonged measurements in blood.

All electrode types exhibit time-dependent drift in bovine blood, consistent with prior reports of EAB sensor behavior in complex biological matrices [65, 68, 70]. The unroughened gold wire controls show a gradual positive drift, while the roughened gold wire controls exhibit a larger monotonic increase in signal over time. This enhanced drift in roughened electrodes is attributed to their higher electrochemically active surface area, which increases susceptibility to protein adsorption, surface restructuring, and gradual changes in electron-transfer pathways[59, 70].

However, the 1500μm planar microelectrodes display an initial increase in signal followed by a pronounced negative drift over longer timescales. This behavior likely reflects

a combination of surface fouling, partial degradation of the self-assembled monolayer, and changes in effective aptamer dynamics at the planar electrode interface[47, 65, 70]. Similar bidirectional drift behavior has been reported previously for planar gold electrodes operated in serum and whole blood environments[65, 71].

Importantly, although the absolute signals drift significantly over time, these changes are largely frequency-independent, affecting both signal-on and signal-off frequencies in a correlated manner. This observation motivates the use of KDM, which suppresses common-mode drift by combining frequency-paired signals [63, 65, 66]. As demonstrated in earlier sections, KDM enables robust polymyxin B quantification even under conditions where absolute signal drift would otherwise limit sensor performance.

Overall, these overnight measurements show that EAB sensors can drift over time when operated in blood, which makes long-term measurements challenging. However, they also demonstrate that using differential, frequency-based measurement methods is important because it helps maintain stable and reliable sensor performance in complex biological environments.

A key finding from the results is that the MEAs can be functionalized with aptamers without requiring electrochemical surface roughening while still producing KDM responses comparable to electrochemically roughened gold wire control electrodes. The planar microelectrodes exhibited robust, target-dependent KDM behavior across measurements, indicating that effective differential signaling can be achieved on microfabricated platforms without additional surface modification steps. This demonstrates that electrochemical roughening is not a prerequisite for achieving high-quality KDM performance in planar EAB sensors. Importantly, this simplifies sensor fabrication and improves compatibility with lithographic processing, supporting the use of planar MEAs for scalable and multiplexed EAB sensing applications.

Chapter 4

Summary and Outlook

The main goal of this thesis is to advance EAB sensing by developing scalable device architectures capable of multi-site and spatially resolved molecular measurements. Planar gold microelectrode array (MEA) platforms were designed, fabricated, and characterized as an alternative to conventional single-site electrochemical sensor configurations.

The fabrication workflow, device interfacing, and electrochemical characterization of these MEAs have been systematically presented, with emphasis on reproducibility and compatibility with aptamer functionalization. First, the design and microfabrication of planar gold MEAs using standard fabrication techniques were shown. Precise control over electrode geometry and passivation enabled stable and reproducible electrochemical behavior, as confirmed by electrochemical measurement. A custom PCB interface was developed to enable reliable electrical connections to external instrumentation.

Subsequent application of these MEAs to EAB sensing showed that square-wave voltammetry responses, binding-dependent signal changes, and drift characteristics are comparable to those observed in conventional gold wire electrode EAB sensors, particularly when kinetic differential measurements were employed.

This thesis also establishes that planar gold microelectrode arrays support effective EAB

sensing without requiring electrochemical surface roughening. Aptamer-functionalized planar microelectrodes were shown to produce kinetic differential measurement (KDM) responses comparable to those observed on electrochemically roughened gold wire control electrodes.

For future work, increasing electrode density and reducing device dimensions will be necessary to enable spatially resolved pharmacokinetic measurements in biologically relevant environments.The use of BCB passivation aligns the present MEA platform with established implantable microsystem technologies, enabling future translation toward chronic or in vivo electrochemical sensing applications. Further investigation of long-term stability and biofouling effects in complex media, along with optimization of surface chemistries and interrogation conditions, will be required. Integration of on-board amplification and multiplexed readout electronics near the sensing sites represents an important step toward minimally invasive, real-time, continuous in vivo molecular monitoring.

Bibliography

[1] V. Naresh and N. Lee. "A Review on Biosensors and Recent Development of Nanostructured Materials-Enabled Biosensors". In: *Sensors* 21 (2021), p. 1109.

[2] International Union of Pure and Applied Chemistry. "Glossary for Chemists of Terms Used in Biotechnology (IUPAC Recommendations 1992)". In: *Pure and Applied Chemistry* 64.1 (1992), pp. 143–168. DOI: 10.1351/pac199264010143.

[3] N. Bhalla et al. "Introduction to Biosensors". In: *Essays in Biochemistry* 60 (2016), pp. 1–8.

[4] W. R. Heineman and W. B. Jensen. "Leland C. Clark Jr. (1918–2005)". In: *Biosensors and Bioelectronics* 21 (2006), pp. 1403–1404.

[5] N. Reddy, N. Verma, and K. Dungan. *Monitoring Technologies—Continuous Glucose Monitoring, Mobile Technology, Biomarkers of Glycemic Control*. Endotext, 2000.

[6] D. Grieshaber et al. "Electrochemical Biosensors—Sensor Principles and Architectures". In: *Sensors* 8 (2008), pp. 1400–1458.

[7] Y. Wu, R. D. Tilley, and J. J. Gooding. "Challenges and Solutions in Developing Ultrasensitive Biosensors". In: *Journal of the American Chemical Society* 141 (2019), pp. 1162–1170.

[8] D. Wei et al. "Electrochemical Biosensors at the Nanoscale". In: *Lab on a Chip* 9 (2009), pp. 2123–2131.

[9] M. Cui et al. "A Label-Free Electrochemical DNA Biosensor for Breast Cancer Marker BRCA1 Based on Self-Assembled Antifouling Peptide Monolayer". In: *Sensors and Actuators B: Chemical* 244 (2017), pp. 742–749.

[10] P. Dauphin-Ducharme and K. W. Plaxco. "Maximizing the Signal Gain of Electrochemical-DNA Sensors". In: *Analytical Chemistry* 88 (2016), pp. 11654–11662.

[11] N. Arroyo-Currás et al. "Subsecond-Resolved Molecular Measurements in the Living Body Using Chronoamperometrically Interrogated Aptamer-Based Sensors". In: *ACS Sensors* 3 (2018), pp. 360–366.

[12] K. Brown et al. "Utilization of an Electrochemiluminescence Sensor for Atropine Determination in Complex Matrices". In: *Analytical Chemistry* 91 (2019), pp. 12369–12376.

[13] S. J. Smith, C. R. Nemr, and S. O. Kelley. "Chemistry-Driven Approaches for Ultrasensitive Nucleic Acid Detection". In: *Journal of the American Chemical Society* 139 (2017), pp. 1020–1028.

[14] S. O. Kelley. "Advancing Ultrasensitive Molecular and Cellular Analysis Methods to Speed and Simplify the Diagnosis of Disease". In: *Accounts of Chemical Research* 50 (2017), pp. 503–507.

[15] M. Gebala and W. Schuhmann. "Understanding Properties of Electrified Interfaces as a Prerequisite for Label-Free DNA Hybridization Detection". In: *ChemPhysChem* 11 (2010), pp. 2887–2895.

[16] W. Zhou et al. "Aptamer-Based Biosensors for Biomedical Diagnostics". In: *Analyst* 139 (2014), p. 2627.

[17] A. M. Downs and K. W. Plaxco. "Real-Time, In Vivo Molecular Monitoring Using Electrochemical Aptamer-Based Sensors: Opportunities and Challenges". In: *ACS Sensors* 7 (2022), pp. 2823–2832.

[18] Emmanuel Ramirez et al. "A Wearable System for Wireless and Multiplexed Molecular Sensing Via Solid Microneedles". In: Jan. 2025, pp. 383–386. DOI: 10.1109/MEMS61431.2025.10918177.

[19] Y. Wu et al. "Using Spectroscopy to Guide the Adaptation of Aptamers into Electrochemical Aptamer-Based Sensors". In: *Bioconjugate Chemistry* 34.1 (2023), pp. 124–132. DOI: 10.1021/acs.bioconjchem.2c00275.

[20] V. S. Polikov, P. A. Tresco, and W. M. Reichert. "Progress towards biocompatible intracortical microelectrodes". In: *Biomaterials* 26.17 (2005), pp. 5369–5377.

[21] K. D. Wise, J. B. Angell, and A. Starr. "An Integrated-Circuit Approach to Extracellular Microelectrodes". In: *IEEE Transactions on Biomedical Engineering* 17 (1970), pp. 238–247.

[22] K. D. Wise. "Silicon Microsystems for Neuroscience and Neural Prostheses". In: *IEEE Engineering in Medicine and Biology Magazine* 24 (2005), pp. 22–29.

[23] S. Herwik et al. "Fabrication Technology for Silicon-Based Microprobe Arrays Used in Acute and Sub-Chronic Neural Recording". In: *Journal of Micromechanics and Microengineering* 19 (2009), p. 074008.

[24] P. K. Campbell et al. "A Silicon-Based, Three-Dimensional Neural Interface: Manufacturing Processes for an Intracortical Electrode Array". In: *IEEE Transactions on Biomedical Engineering* 38 (1991), pp. 758–768.

[25] M. A. L. Nicolelis et al. "Chronic, Multisite, Multielectrode Recordings in Macaque Monkeys". In: *Proceedings of the National Academy of Sciences of the USA* 100 (2003), pp. 11041–11046.

[26] E. McGlynn, A. M. Norcia, and D. Palanker. "Flexible and Wireless Implantable Neural Electronics". In: *Annual Review of Biomedical Engineering* 23 (2021), pp. 367–400.

[27] S. K. Kelly et al. "A Hermetic Wireless Subretinal Neurostimulator for Vision Prostheses". In: *IEEE Transactions on Biomedical Engineering* 58.11 (Nov. 2011), pp. 3197–3205.

[28] A. Uddin et al. "Wafer-Scale Integration of CMOS Chips for Biomedical Applications via Self-Aligned Masking". In: *IEEE Transactions on Components, Packaging and Manufacturing Technology* 1.10 (Oct. 2011), pp. 1542–1550.

[29] National Institutes of Health. *Neural Interfaces: Research and Clinical Applications*. Tech. rep. Bethesda, MD, USA: National Institutes of Health, 2008.

[30] T. Stieglitz, H. Beutel, and J.-U. Meyer. "Microflex—A flexible neural probe with integrated microsystems". In: *Sensors and Actuators A: Physical* 83 (2000), pp. 8–14.

[31] Marc J. Madou. *Fundamentals of Microfabrication and Nanotechnology*. 3rd ed. Boca Raton, FL, USA: CRC Press, 2011. ISBN: 978-1420065173.

[32] Sami Franssila. *Introduction to Microfabrication*. 2nd ed. Hoboken, NJ, USA: Wiley, 2010. ISBN: 978-0470749838.

[33] *Lift-Off Techniques: Microfabrication Process Notes*. Internal process documentation describing pre-development toluene soak for improved photoresist profile and metal lift-off. URL: `https://wiki.nanofab.ucsb.edu/w/images/b/bc/Liftoff-Techniques.pdf`.

[34] B. Rubehn and T. Stieglitz. "In vitro evaluation of the long-term stability of polyimide as a material for neural implants". In: *Journal of Neural Engineering* 7.3 (2010), p. 036007.

[35] Dow Chemical Company. *CYCLOTENE™ 3000 Series Advanced Electronic Resins: Processing Guide*. Rev. A. 2010.

[36] K. D. Wise et al. "Microelectrodes, microelectronics, and implantable neural microsystems". In: *Proceedings of the IEEE* 96.7 (2008), pp. 1184–1202.

[37] Transene Company, Inc. *Aluminum Etchant Type A: Technical Data Sheet*.

[38] J. W. Coburn and E. Kay. "Reactive ion etching of polymers". In: *Journal of Applied Physics* 43.12 (1972), pp. 4965–4971.

[39] C. A. Mack. "Selective plasma etching of polymer dielectrics". In: *Journal of Vacuum Science & Technology B* 20.4 (2002), pp. 1352–1360.

[40] Transene Company, Inc. *Chromium Etchant 1020: Technical Data Sheet*.

[41] S. Franssila and S. Sainiemi. "Pattern transfer in deep silicon etching". In: *Journal of Vacuum Science & Technology B* 23.6 (2005), pp. 2240–2246.

[42] K. Sarakinos, J. Alami, and S. Konstantinidis. "High power pulsed magnetron sputtering: A review on scientific and engineering state of the art". In: *Surface and Coatings Technology* 204 (2010), pp. 1661–1684.

[43] F. Laermer and A. Schilp. "Method of anisotropically etching silicon". US5501893. 1996.

[44] R. J. White and K. W. Plaxco. "Exploiting binding-induced changes in probe flexibility for the optimization of electrochemical biosensors". In: *Analytical Chemistry* 82.1 (2010), pp. 73–76.

[45] Allen J. Bard and Larry R. Faulkner. *Electrochemical Methods: Fundamentals and Applications*. 2nd ed. New York, NY, USA: Wiley, 2001. ISBN: 978-0471043720.

[46] Y. Xiao et al. "On the signaling of electrochemical aptamer-based sensors: Collision- and folding-based mechanisms". In: *Electroanalysis* 21.11 (2009), pp. 1267–1271.

[47] M. Aller Pellitero et al. "Os(II/III) redox reporters enable pH-insensitive electrochemical DNA-based sensing". In: *Analyst* 148 (2023), pp. 806–813.

[48] B. R. Baker et al. "An electronic aptamer-based small-molecule sensor for the rapid, label-free detection of cocaine in biological fluids". In: *Journal of the American Chemical Society* 128.10 (2006), pp. 3138–3139.

[49] R. L. Nation et al. "Polymyxins: Clinical pharmacology and toxicology". In: *The Lancet Infectious Diseases* 15.2 (2015), pp. 225–234.

[50] J. Zavascki et al. "Polymyxin B for the treatment of multidrug-resistant pathogens". In: *Clinical Infectious Diseases* 47.3 (2008), pp. 343–349.

[51] J. Abodakpi, R. Nation, and J. Li. "Plasma protein binding of polymyxin B". In: *Antimicrobial Agents and Chemotherapy* 59.10 (2015), pp. 6592–6599.

[52] Y. Xiao et al. "Label-free electronic detection of thrombin in blood serum by using an aptamer-based sensor". In: *Journal of the American Chemical Society* 127.51 (2005), pp. 17990–17991.

[53] R. J. White, A. A. Rowe, and K. W. Plaxco. "Re-engineering aptamers to support reagentless, self-reporting electrochemical sensors". In: *Analyst* 135.3 (2010), pp. 589–594.

[54] L. R. Schoukroun-Barnes, J. Wagan, and R. J. White. "Enhancing the analytical performance of electrochemical RNA aptamer-based sensors". In: *Analytical Chemistry* 86.22 (2014), pp. 1131–1137.

[55] R. Y. Lai, K. W. Plaxco, and A. J. Heeger. "Aptamer-based electrochemical detection of picomolar platelet-derived growth factor directly in blood serum". In: *Analytical Chemistry* 79.1 (2007), pp. 229–233.

[56] J. S. Swensen et al. "Continuous, real-time monitoring of cocaine in undiluted blood serum via a microfluidic, electrochemical aptamer-based sensor". In: *Journal of the American Chemical Society* 131.12 (2009), pp. 4262–4266.

[57] S. Trasatti and O. A. Petrii. “Real surface area measurements in electrochemistry”. In: *Pure and Applied Chemistry* 63.5 (1991), pp. 711–734.

[58] R. J. White, A. A. Rowe, and K. W. Plaxco. “Optimization of electrochemical aptamer-based sensors via optimization of probe packing density and surface chemistry”. In: *Langmuir* 24.18 (2008), pp. 10513–10518.

[59] A. M. Downs et al. “Nanoporous gold for the miniaturization of in vivo electrochemical aptamer-based sensors”. In: *ACS Sensors* 6.6 (2021), pp. 2299–2306.

[60] S. Li et al. “A wrinkled structure of gold film greatly improves the signaling of electrochemical aptamer-based biosensors”. In: *RSC Advances* 11 (2021), pp. 671–677.

[61] Evelyn Adela Carreto Guevara. “Aptamer Selection and Development of Electrochemical Aptamer-Based Sensors for Neuropeptide Y”. PhD thesis. Lincoln, NE, USA: University of Nebraska–Lincoln, Aug. 2025. URL: `https://digitalcommons.unl.edu/chemistrydiss/117/`.

[62] A. M. Downs et al. “Improved calibration of electrochemical aptamer-based sensors”. In: *Scientific Reports* 12 (2022), p. 5535.

[63] E. Verrinder et al. “Comparison of voltammetric methods used in the interrogation of electrochemical aptamer-based sensors”. In: *Sensors & Diagnostics* 3 (2024), pp. 95–103.

[64] A. E. Radi et al. “Reagentless, reusable, ultrasensitive electrochemical molecular beacon aptasensor”. In: *Journal of the American Chemical Society* 128.1 (2006), pp. 117–124.

[65] K. K. Leung et al. “Elucidating the mechanisms underlying the signal drift of electrochemical aptamer-based sensors in whole blood”. In: *ACS Sensors* 6.9 (2021), pp. 3340–3347.

[66] N. Arroyo-Currás et al. “High surface area electrodes generated via electrochemical roughening improve the signaling of electrochemical aptamer-based biosensors”. In: *Analytical Chemistry* 89.22 (2017), pp. 12185–12191.

[67] N. Singh et al. “Cortisol detection in undiluted human serum using an electrochemical structure-switching aptamer”. In: *ACS Omega* 6.42 (2021), pp. 27888–27897.

[68] B. S. Ferguson et al. “Real-time, aptamer-based tracking of circulating therapeutic agents in living animals”. In: *Science Translational Medicine* 5.213 (2013), 213ra165.

[69] E. Verrinder et al. “Dual-frequency ratiometric approaches to electrochemical aptamer-based sensor interrogation”. In: *ACS Sensors* 9.3 (2024), pp. 3205–3211.

[70] Z. Watkins et al. “Week-long operation of electrochemical aptamer sensors in serum”. In: *ACS Sensors* 8.3 (2023), pp. 1119–1131.

[71] Douglas C. Montgomery. *Design and Analysis of Experiments*. 9th ed. Hoboken, NJ, USA: Wiley, 2017.

[72] P. Dauphin-Ducharme et al. "Electrochemical aptamer-based sensors for improved therapeutic drug monitoring". In: *ACS Sensors* 4.11 (2019), pp. 2832–2837.

[73] A. Shaver et al. "Optimization of vancomycin aptamer sequence length increases sensitivity of electrochemical aptamer-based sensors". In: *ACS Sensors* 7.12 (2022), pp. 3895–3905.

[74] J. W. Tukey. "Comparing individual means in the analysis of variance". In: *Biometrics* 5.2 (1949), pp. 99–114.

[75] H. Abdi and L. J. Williams. "Tukey's honestly significant difference (HSD) test". In: *Encyclopedia of Research Design*. Ed. by N. Salkind. Vol. 3. Sage, 2010, pp. 1–5.